UC Santa Cruz

UC Santa Cruz Electronic Theses and Dissertations

Title

Characterization of an airflow solar window

Permalink

https://escholarship.org/uc/item/71w4c94q

Author

Chialastri, Andrea

Publication Date

2017

Peer reviewed|Thesis/dissertation

eScholarship.org Powered by the California Digital Library
University of California

UNIVERSITY OF CALIFORNIA
SANTA CRUZ

CHARACTERIZATION OF AN AIRFLOW SOLAR WINDOW

A thesis submitted in partial satisfaction
of the requirements for the degree of

MASTER OF SCIENCE

in

ELECTRICAL ENGINEERING

by

Andrea Chialastri

June 2017

The Thesis of Andrea Chialastri
is approved:

_____
Professor Michael Isaacson, Chair

_____
Professor Patrick E. Mantey

_____
Professor Leila Parsa

_____
Tyrus Miller
Vice Provost and Dean of Graduate Studies

Copyright © by

Andrea Chialastri

2017

Table of Contents

List of Figures

List of Tables

Abstract

Characterization Of An Airflow Solar Window

by

Andrea Chialastri

Integrated building elements, which combine their structural and architectural functions with that of energy generation, are expected to become increasingly important in the future scenario of energy efficient buildings, and they could significantly contribute to the thermal behaviour of the building envelope in order to provide energy savings. A prototype of a building-integrated photovoltaic/ thermal (BIPV/T) solar air collector has been built by a Palo Alto start-up company, and consists on a double pane airflow window wall with photovoltaic (PV) louvers embedded in it. The unit is intended to perform the functions of both thermal and electrical generation, as well as light transmission and shading control. In this work, the prototype's performance has been tested in different outdoor conditions and under different airflow speeds, with the aim of investigating its thermal and electrical capabilities. The results presented in this thesis showed an optimal behaviour during the winter, with a maximum air temperature rise (from bottom to top) of about 30°C and average thermal efficiency of 31%. By using inexpensive PV modules with a rated efficiency of 12.5%, an actual electrical efficiency of 7% was recorded under the maximum operating temperatures.

Acknowledgements

First and foremost I wish to express my sincerest gratitude to my advisor, Dr. Michael Isaacson, who has supported me throughout my thesis with his patience and knowledge and steered me in the right the direction whenever he thought I needed it, whilst allowing me the room to work in my own way. His guidance helped me in all the time of research and writing of this thesis, and I could not have imagined having a better advisor and mentor.

A very special thanks goes also to Dr. Narinder Singh Kapany, for his continuous motivation and enthusiasm towards my research, and for giving me the opportunity to work in his group in such a creative and stimulating environment. I consider it an honor to have worked with him, and his teachings represented for me both a scientific and a personal growth, and I am deeply grateful for this.

I would like to thank my colleagues and friends from SolarPath: Jake, Josh and Larry Tarter, Andrei Manoliu, Mark Hintzke and Raj Kapany, for the construction of the prototype and the many stimulating and helpful discussions and comments.

I would also like to thank the Hartnell College staff for providing the space to host the equipment and perform the measurements, especially Mike Thomas for his encouragement and friendship that persisted even after my work there.

The most special thanks go to my parents and my brother and sister, for their constant love throughout my entire life, and, of course, to my greatest supporter and life partner, my wife, without whom I would not be the person I am.

Chapter 1

Introduction

1.1 Background

1.1.1 Energy Consumption In Buildings

One of the XXI century's largest and most concerning issues is represented by the radical change and evolution that the world energy system is experiencing, characterized by a shift from a two-hundred-years-old energy system based on fossil fuels towards a more complex scenario, which involves the use of renewable energy sources, distributed generation and smart grids, as well as energy saving and energy efficiency approaches. Buildings account for about 40% of the global energy demand [1], a large part of which is being used for space heating and cooling in both the residential and commercial sector. They also represent a remarkable fraction of the global CO_2 emissions in developed countries, which is about 39% for the U.S., 36% for Europe and 20% for China. Fig 1*a* [2] shows the trend of the U.S. total energy consumption by sector from 1949 to 2016. In the past decade, the energy used by the residential and commercial sectors were around 21% and 18%, respectively. As of February 2017, the energy consumptions in the residential sector (Fig 1*b*) came mainly from natural gas (56%) and electricity (32%), the latter being produced using fossil fuels (56%), nuclear energy (25%) and renewable sources (19%) such as solar, wind, hydroelectric, biomass and geothermal energy (Fig 1*c*).

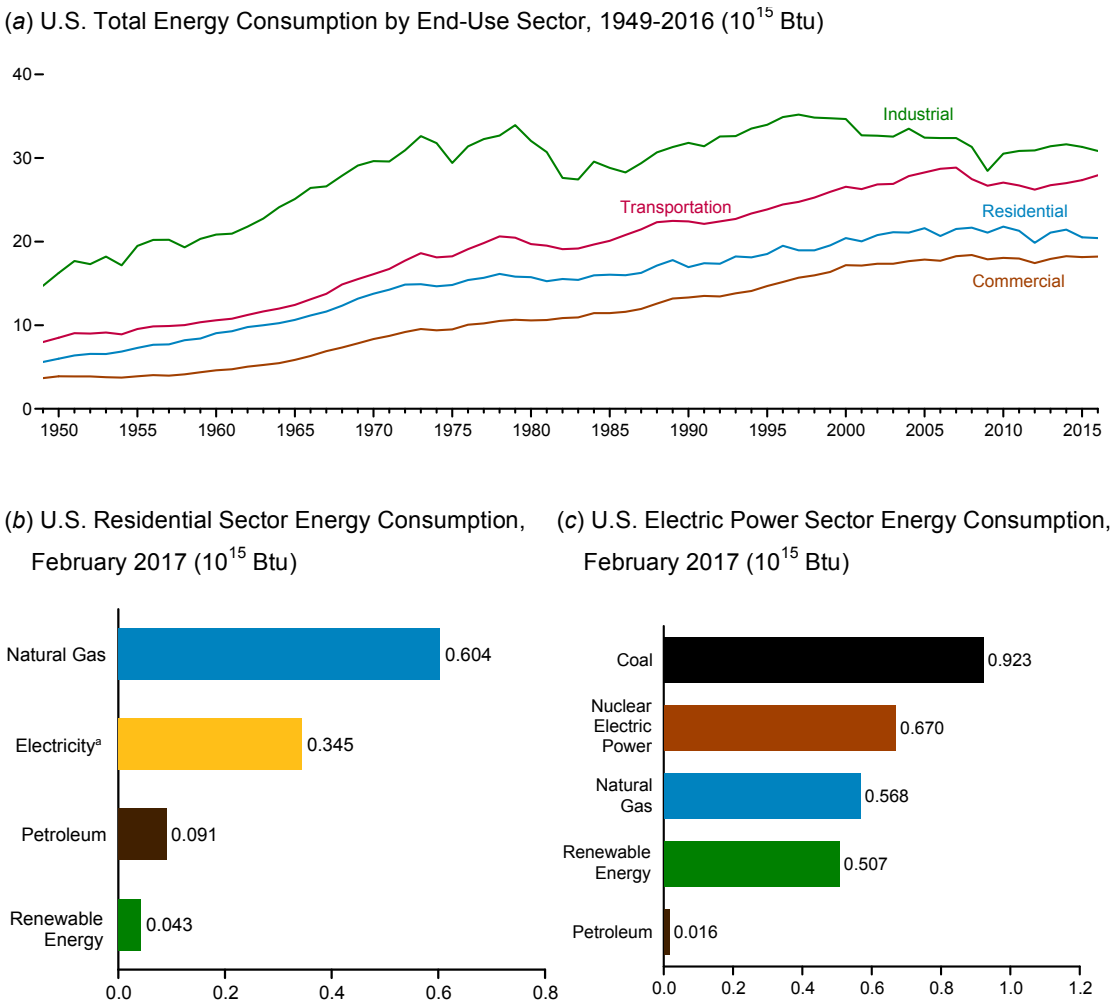

Fig 1: U.S. energy consumption: (a) total energy consumption by end-use sector; (b) residential sector and (c) electric power sector energy consumption by major sources [2].

As shown in Fig 2**,** in the residential sector about 50% of the total energy demand is used for space heating and cooling [3]. This is closely related to the degree of insulation between the building envelope and the environment, and any improvements to the different elements, such as ceiling, floors, walls and windows, would contribute to the overall thermal balance and provide energy savings. As shown in Fig 3, between 35% and 55% of the energy transfer is from floors and ceilings both in summer and

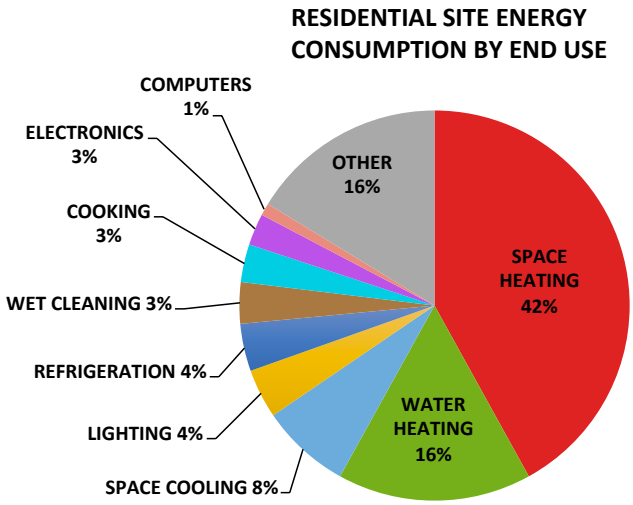

Fig 2: Residential energy consumptions in the U.S. in 2015 [3].

winter, 15% to 25% from walls and the remaining from fenestrations and possible air leakages [4].

Glazed openings such as windows, skylights and curtain walls accounts for 10% to 20% of the total thermal losses in winter, and about one third (25% - 35%) of the heat gain in summer, and the development of new window technologies has been historically a major factor in lowering heating or cooling requirements of buildings.

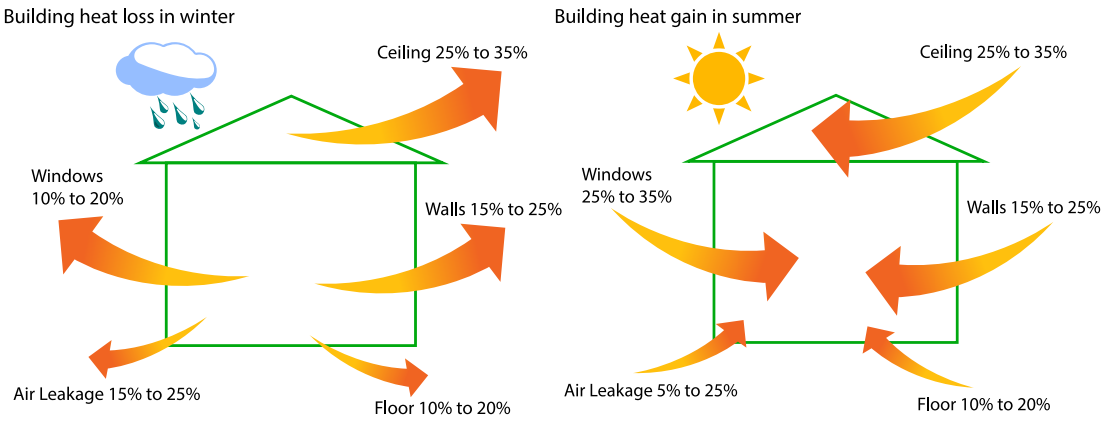

Fig 3: Heat losses and heat gain through the building envelope [4].

1.1.2 Trombe Walls

Many efforts have been made to reduce the energy requirements of buildings by means of sustainable design approaches, some based on active and passive solar systems and techniques, aimed towards what are called “zero net energy” buildings. Among the different technologies for passive solar building design, Trombe walls represent one of the main architectural features that contribute to the ventilation as well as heating and cooling of buildings, and have the potential of reducing energy consumption by up to 30% [5].

As shown in Fig 4, a conventional Trombe wall [7] consists of a glass panel (2) placed in front of a wall painted with a dark heat absorbing material (1), with an air space in between (3). As solar radiation (4) passes through the glass and reaches the wall, the temperature of the latter rises, and heat is slowly transmitted to the inside by conduction through the wall (5). The temperature increase is further enhanced by the

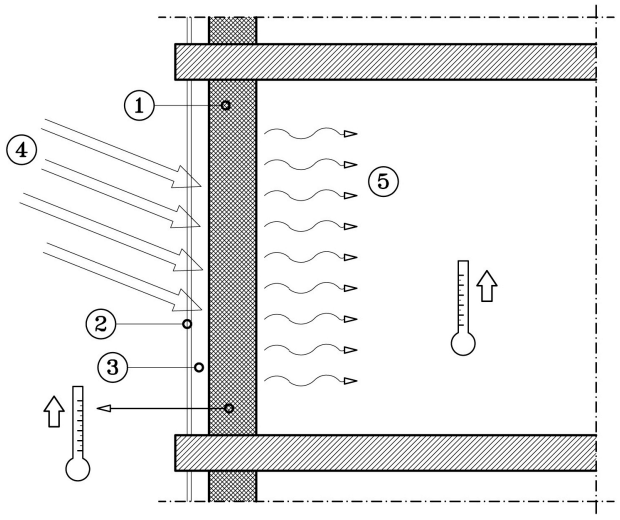

Fig 4: Classic Trombe wall schematics [6].

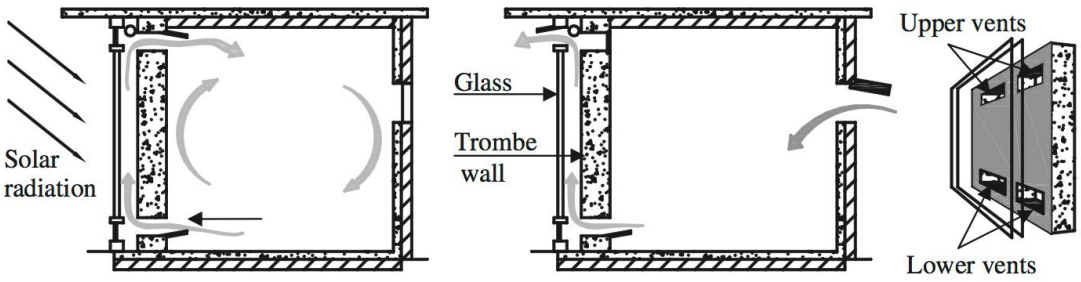

Fig 5: Operation of a vented Trombe wall [8].

glass opacity to the long-wave infrared radiation that the wall surface emits to the outside, which is reflected back by the glass, allowing for more heat to be captured within the air space.

A more efficient variation is realized by means of vents at the bottom and top of the wall, which connect the air space with the inner room, therefore allowing for air circulation (Fig 5). Furthermore, in a vented Trombe wall the temperature gradient that establishes between the cooler air entering from the bottom and the warmer air at the top generates convective currents, so that heat is transferred to the inside by convection as well.

1.1.3 Flat-Plate Solar Thermal Collectors

Solar thermal collectors can be classified in three main categories [9]: flat-plate collectors, consisting of a single encasement rectangular box, evacuated tube collectors, made of parallel glass tubes with vacuum created inside each tube, and concentrating collectors, which are of various shapes and configurations (such as compound parabolic connectors, parabolic trough, linear Fresnel and central tower receiver), and

work by reflecting and concentrating the solar radiation to a focal point. Among the different types of collectors, the flat-plate one is the most widely used and most established and mature technology, especially with regard to domestic hot water heating and space heating applications, and this chapter will give a short overview of this category.

Despite the use of different technologies, flat-plate collectors all share the same working principle, which is the conversion of solar radiation into thermal energy, or heat. This conversion is realized by the absorption of sunlight by a surface, called the absorber, which is in thermal contact with the working fluid (water or air) to which the heat is then transferred and carried out of the collector to be used or stored. The absorber is generally a black-painted surface, as it will have a better absorptivity, which means that a larger fraction of solar radiation is absorbed and converted into heat. The use of spectrally selective materials would further increase the absorption by capturing more radiation in the solar wavelengths range (visible and near-infrared) while limiting the radiation reemitted from the absorber in the long-wave infrared range. The solar spectrum is indeed composed of 3 main spectral bands: about 6.4% of the energy is within 250-380 nm (UV light), a large part of the radiation (around 48%) is emitted as visible light in the range of 380-780 nm and the remaining 45.6% as near-infrared radiation, in a range of wavelengths ranging between 780nm and 2.5 μm [10].

1.1.3.1 Liquid Type Collectors

Liquid-based flat plate solar collectors consist of a selective absorber plate, generally made of copper or aluminum, a parallel or serpentine tube structure where the heat-transfer fluid flows, a cover (glass or plastic) to reduce convective losses to the environment, a thermal-insulating material on the bottom and sides of the collector to limit conduction losses, and a sheet metal-case [11]. A schematic representation of a typical collector's cross-section is shown in Fig 6. As the solar radiation reaches the absorber, it is converted into heat, which is then transferred through the pipes to the fluid, resulting in a temperature increase of the latter. The most commonly used liquid is water, which is mixed with glycol for applications in cold climates where the temperatures are likely to drop below freezing conditions.

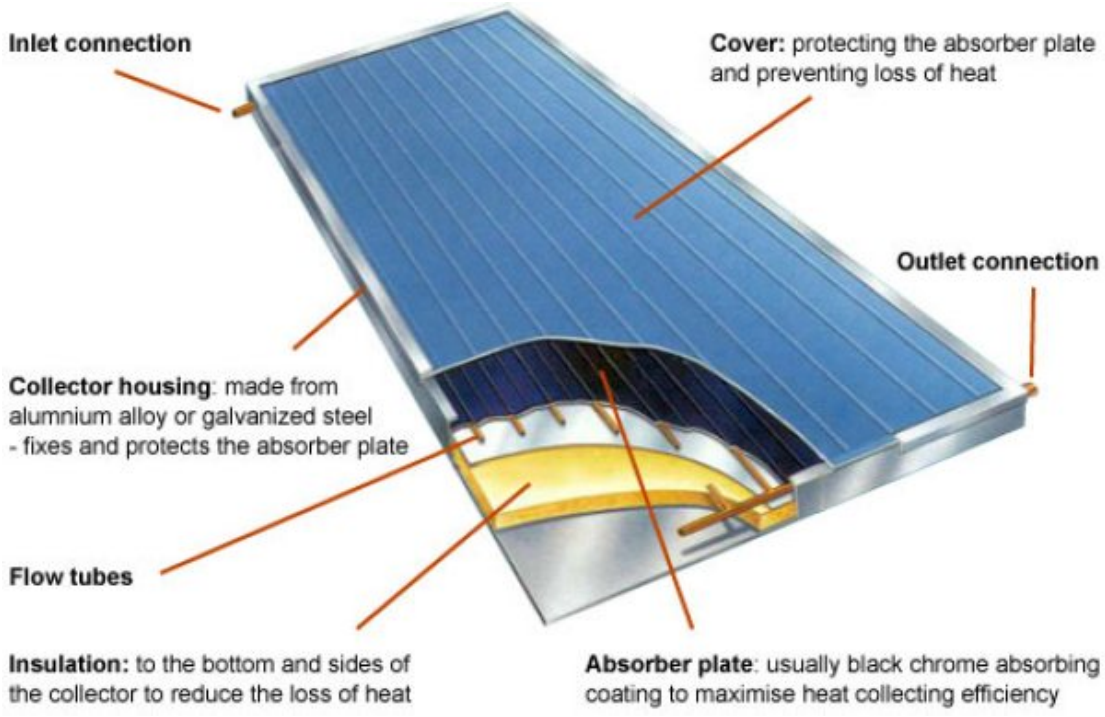

Fig 6: Solar water collector [12].

Liquid flat-plate collectors are a simple and reliable technology, which is readily available, have no moving parts and are easy to install. Although they have a good cost-to-performance ratio, they are limited in temperature levels below 100 °C, as the efficiency drops significantly at higher temperatures due to increased heat losses. Typical temperature range is 40 - 80 °C for regular collectors [13], which makes them well suited for domestic hot water generation applications.

1.1.3.2 Air Type Collectors

Solar air collectors have a similar construction to that of liquid flat plate collectors, but they use air as the heat transfer fluid instead of water. They can be classified depending on the different path the air enters in contact with the absorber (Fig 7) [14]. The flow can be above the absorber that is located down on the back insulation, and although it is the simplest design it is also the least efficient, since the air directly transfers the heat to the glass cover, and therefore the convective losses are higher. This can be overcome by having the air flowing under the absorber, which can be manufactured with fins to increase the heat transfer area. Having the flow on both the

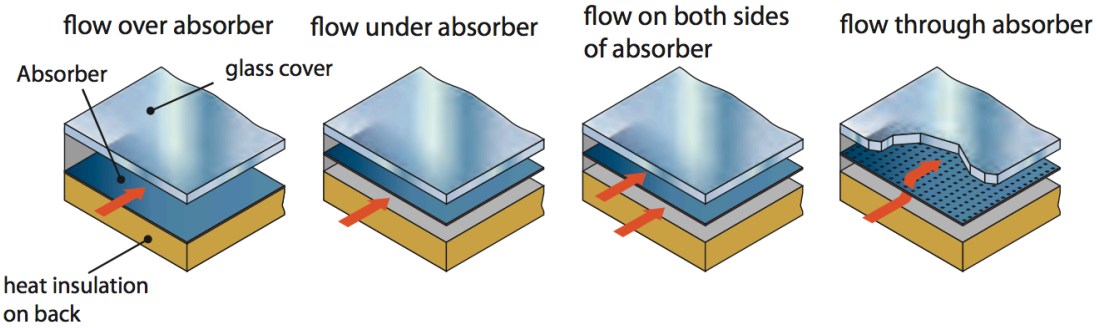

Fig 7: Different airflow patterns in solar air collectors [14].

top and the bottom side of the absorber further enhances the heat transfer from the absorber to the air [15], even if this would reintroduce thermal losses through the glass cover. A more recent design uses an absorber made of a porous plate, through which the air flows, and it represents the configuration with the highest heat transfer rate, but the downside is a higher pressure drop across the collector, which requires more power for the fans circulating the air. [14]. A schematic of a typical commercial air collector is shown in Fig 8, where the absorber is composed of individual channels where the air flows.

There are several advantages and disadvantages in using air as heat-transfer fluid instead of water [16]. Air collectors have generally a simpler construction, due to the fact that there are no water-leakage problems and no freezing or boiling problems, therefore no protection is necessary. Air is also non-corrosive, and that implies less

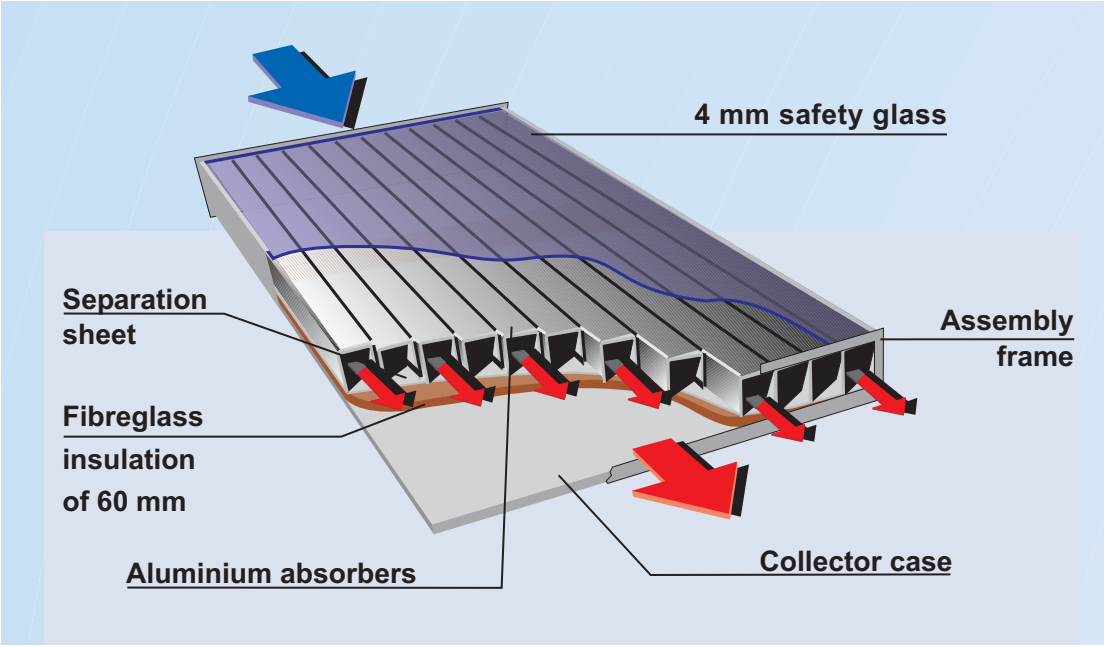

Fig 8: Schematics of a solar air collector (Source: Grammer Solar GmbH, Germany).

maintenance and an increased collector life, as well as the possibility to safely feed the air directly into a heated room, in which case the air collector can also be integrated with the building ventilation system as a means of supplying fresh heated air from the outside. On the other hand, air systems require larger ducts than water piping to be installed in a building, as well as more electricity consumption by fans or blowers for ventilation due to the higher pressure drops. Furthermore, the poorer thermal properties involve lower collector efficiencies in comparison to water ones, and also make the transfer of heat to another fluid, such as water for hot water generation, more difficult and requiring larger exchanger surfaces [17].

1.1.3.3 Hybrid PV/T Collectors

A fairly recent development in solar energy technology is represented by a hybrid between photovoltaic modules and solar thermal collectors, in what are referred to as photovoltaic-thermal solar collectors (PV/T) [18]. Here a photovoltaic (PV) module is embedded into a thermal collector, forming a single cogeneration unit for both electrical and thermal conversion.

Commercially-available crystalline silicon PV modules operate operate at efficiencies in the 10-20% range. Of the remaining portion of the non-converted solar radiation, a small fraction (5-10%) is reflected by the glass cover and the rest is converted into heat, which constitutes the major energy output of a PV module. The heat generated contributes to raise the cell temperature by up to 50°C above the ambient [19] if the heat is not removed, resulting in a drop of electrical performances as the temperature

deviates from the standard operating temperature of 25°C [20]. Removing the heat and putting it to use has therefore two main effects: it cools the PV module, allowing it to operate at lower temperatures (and thus more efficiently), and it adds a thermal generation component to the system by having a warm air output [21], which can be used for ventilation, space heating or water heating. When compared to a separate PV module and stand-alone thermal collector, a hybrid PV/T collector generates more energy per unit surface [22], due to the fact that the PV and thermal components share the same support, therefore the same energy (electrical + thermal) could be produced with less surface area, which implies some cost savings. This type of collectors is then well-suited for applications requiring both electricity and heat, and where the available space for collectors' installation is limited.

The PV/T electrical efficiency can either be higher or lower with respect to a regular PV module, and this depends on the impact that additional glass layers could have on the electrical generation (caused by additional absorption and reflection effects) as well as on the capacity that both the glazing and the heat transfer fluid (by providing insulation and heat removal, respectively) have to prevent the module temperature from rising [23]. The thermal efficiency is instead always lower than in the case of a regular thermal collector, and this is due to the non-optimal solar absorption coefficient of PV modules and to the fact that a part of the solar radiation is used to generate electricity.

Hybrid PV/T collectors can use water or air as the heat-transfer fluid, and have a similar construction to that of flat plate modules, with the difference that PV cells can

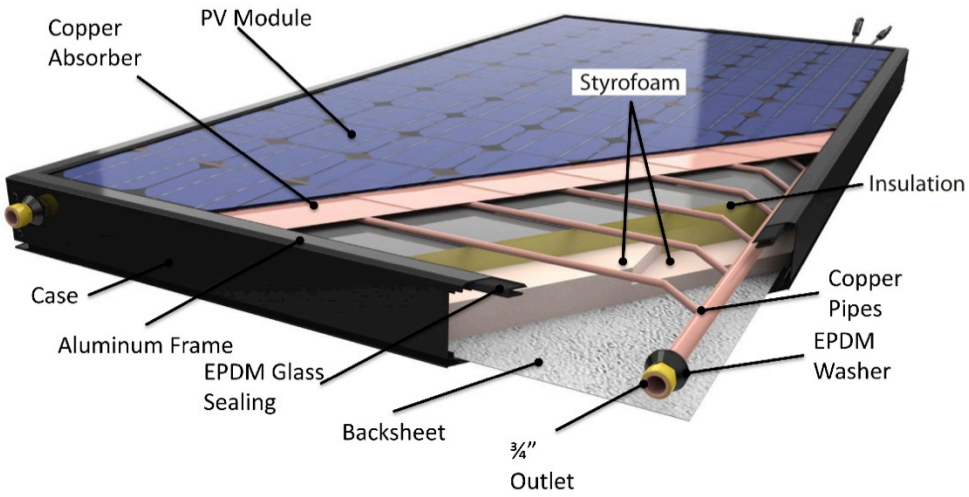

Fig 9: Hybrid PV/T solar collector (source: Solimpeks).

be directly pasted onto the absorber or a PV module can constitute the absorber itself [24]. For a water-based collector, copper pipes are generally placed below the absorber (Fig 9), while in an air-based collector the absorber can be placed in the airflow in the same way as previously discussed in Section 1.1.3.2, with an additional possibility to place the PV module in place of the outer glass cover.

1.2 Project Description

The principal objective of this thesis resides in the characterization and performance evaluation of a prototype of a newly developed Building-Integrated Photovoltaic-Thermal air collector (BIPV/T). The prototype was built by SolarPath Inc., a startup company located in Palo Alto, California, and it is based on a patent (US 8,046,960 B1) by Dr. Narinder Singh Kapany, who invented a new way of integration of photovoltaic systems into building ventilated façades [25].

An experimental investigation has been conducted in Salinas, California, which consisted of a series of electrical and thermal measurements performed under different testing conditions. The recorded data have been used to evaluate the energy generation capabilities and performances of the prototype, with the aim of determining the integration feasibility of this component into the energy system of both residential and commercial buildings.

In this chapter, a brief overview of the patent and a description of the actual prototype will be provided.

1.2.1 The Solar Window Concept

An evolution of the Trombe wall is represented by the invention of a new type of solar window patented by the Indian-born American physicist Dr. Narinder Singh Kapany, which integrates this concept with those of building integrated photovoltaics

(BIPV) and hybrid PV/T collectors, further extending it to building fenestrations such as windows and window walls.

The invention is shown in Fig 10. It consists of a double pane window, where a bottom and a top vent are realized to host fans and air filters (elements 170 and 175 in Fig.10), allowing air to circulate through the cavity (120) between the two glass panes and be filtered. Photovoltaic cells (140) mounted on louvers (145) can be placed in the cavity, which perform the multiple functions of providing shading control, gener-

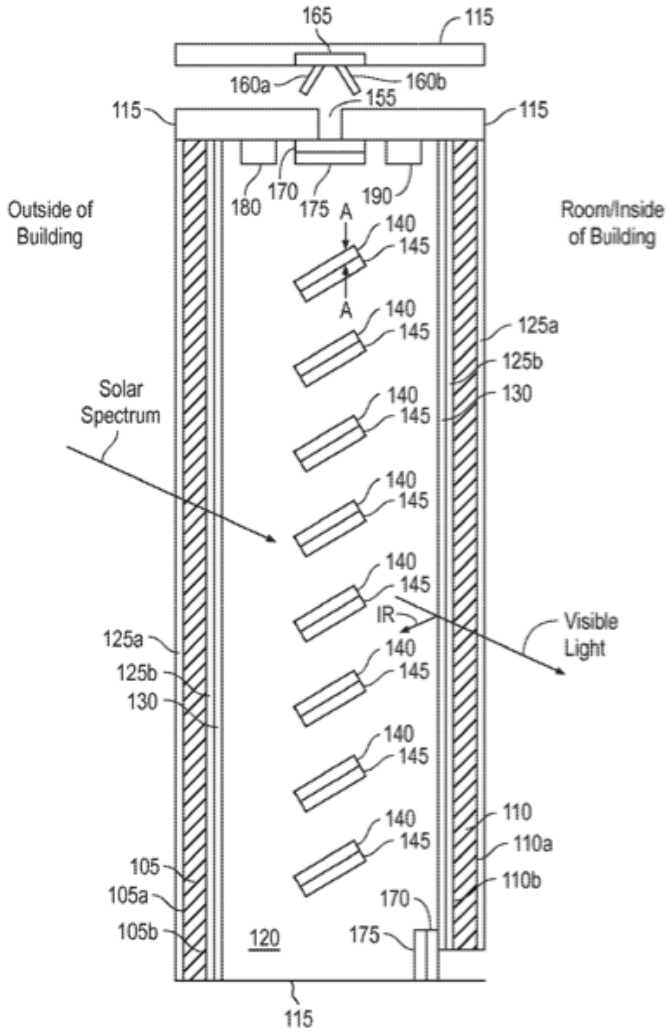

Fig 10: Solar window concept [25].

ating electricity and converting the remaining absorbed fraction of the incoming solar radiation into heat. The latter is then transferred from the PV louvers to the air that circulates from bottom to top and carried out of the window through the top vent, so that it can be either put into use or expelled outside by optional shutters (160a and 160b), which could be controlled by a thermostat (165) that determines whether to let the air entering or exiting the building, depending on the actual room temperature.

The two glass panels are can be coated with anti-reflective layers (125a and 125b in Fig 10) on both sides to reduce reflective losses, and infrared reflective coatings (130) could also be placed on the inner sides facing the cavity, in order to reach maximum heat gain within the air gap by reflecting back the long-wave infrared radiation emitted by the PV louvers.

The patent includes also the possibility of having a thermoelectric generator (180) at the top for additional conversion of heat into electricity, as well as a water heating unit (190) that transfers the heat to a water circuit which is fed from the outside of the window.

1.2.2 The Solar Window Prototype

A first prototype that is based on the aforementioned concept was constructed, featuring most of the elements included in Dr. Kapany's patent. The prototype is shown in Fig 11, and consists of 2 double glazed window compartments with an air cavity in between, held together by an aluminum frame.

Fig 11: Solar window prototype.

Table 1: Prototype geometrical characteristics.

Width	*0.91 m*	*Bottom vent area*	*411.78 cm^2*
Height	*2.92 m*	*Top vent area*	*248.5 cm^2*
Depth	*10.2 cm*	*Parallax module dimensions*	*12.5 x 6.3 cm*
Total gross area	*2.67 m^2*	*Parallax module area*	*78.75 cm^2*
Total glazed area	*1.958 m^2*	*Total top PV array area*	*0.4725 m^2*
Top glazing area	*0.658 m^2*	*BP Solar SX 170B area*	*1.258 m^2*

The principal geometrical characteristics of the prototype are reported in Table 1. The first lower section of the frame hosts the input vent, which in this case is realized on the outer side of the window, allowing the window to operate in what is called "air-supply mode", where fresh ambient air is supplied to the inside of the building and therefore contributes to fulfill ventilation requirements. The vent consists of two apertures of 5.79 x 35.56 cm each, and a metal grid and aluminum fins act as an air filter,

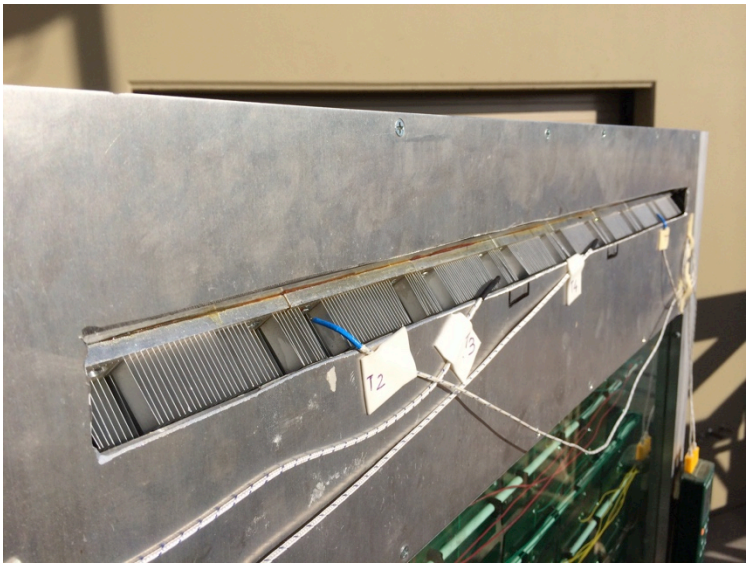

Fig 12: Photograph of the top vent.

preventing dust from entering the window. The output vent, shown in Fig 12, is located at the top section on the back of the unit, and it is a single aperture with dimensions of about 3.5 x 71 cm. The forced ventilation is realized by 10 Sunon KDE1208PTB1-6(OC) computer fans with an operating voltage range of 5-13.8 V and rated power of 2.6 W each at 12 VDC, which are placed inside the top section of the frame as well. A heat exchanger is located downstream of the fans, and it is composed of a U-shaped copper pipe and aluminum fins that are in thermal contact through a metal plate to which they are welded. The pipe runs down along the left side of the window (with respect to a front view), and ends in a storage tank containing glycol and a 65 W water pump to circulate it. This allows the heat to be transferred to a fluid circuit that could be used for radiant floor heating or to preheat water during the summer months when the heat is most needed for domestic hot water production. Fig 13 shows two pictures of the fans and heat exchanger components.

The two main middle sections consist of the double glazed air cavities, which enclose a fixed regular PV module at the bottom and a movable PV array at the top. In the bottom compartment, which has an aperture of 1.3 m^2, a BP Solar SX170B photovoltaic module has been installed, that is rated at 170 W with a nominal efficiency of 13.5%. The top double-glazing encloses an array of 60 Parallax XHHOO1-4 PV modules, which are mounted on 10 plastic rods (holding 6 modules each) that can be manually tilted up to 25° with respect to the normal to the modules. The Parallax modules' electrical specifications are reported in Fig 14.

The PV array makes the top part of the prototype into what can be defined

Fig 13: Fans and heat exchanger at the top of the unit.

more properly as a window, as it allows visibility through it, while the bottom section enclosing a regular photovoltaic module looks more like a solar wall. The original reason of using this type of layout instead of a full PV array on the whole window was to test the maximum absorbing capability of the PV surfaces, which in this case act as thermal absorbers, and are the central component of the system. The BP Solar module contributes to the overall thermal performances but it was not included in the electrical measurements, which were carried out on the PV array alone, as the final product is intended to look like a window on the entire height.

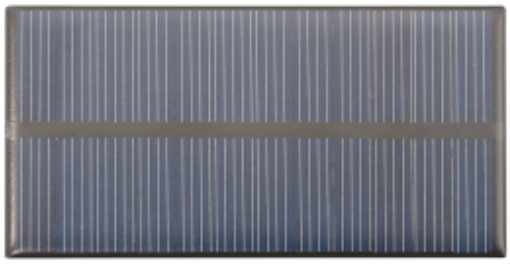

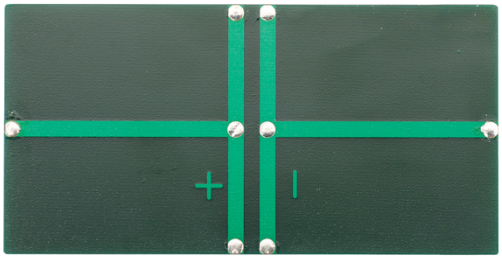

Electrical specifications - XHHOO1-4	
Rated power	*1 W*
Open circuit voltage	*7.2 V*
Short circuit current	*183 mA*
Max power voltage	*6 V*
Max power current	*166 mA*
Operating temperature	*0 – 70 °C*
Number of cells	*12*

Fig 14: Parallax XHHOO1-4 module: front (top left) and back (top right), and its electrical characteristics.

Fig 15: Air passages and tilting of the PV array.

The transition between the different sections of the window is realized through the use of holes into the aluminum shell, in order to allow for air circulation and connect the two air cavities. The fans move the outside ambient air from the bottom vent into the double glazing, where it flows over the PV hot surfaces heated by the solar radiation, and carries the transferred heat up in its rising motion towards the top output vent. Fig 15 shows a close-up of the PV array where the passages interconnecting the different sections can be seen, along with the tilting mechanism on one side of the window, while a schematic of the cross sectional view of the window, with the airflow path represented, is represented in Fig 16**.**

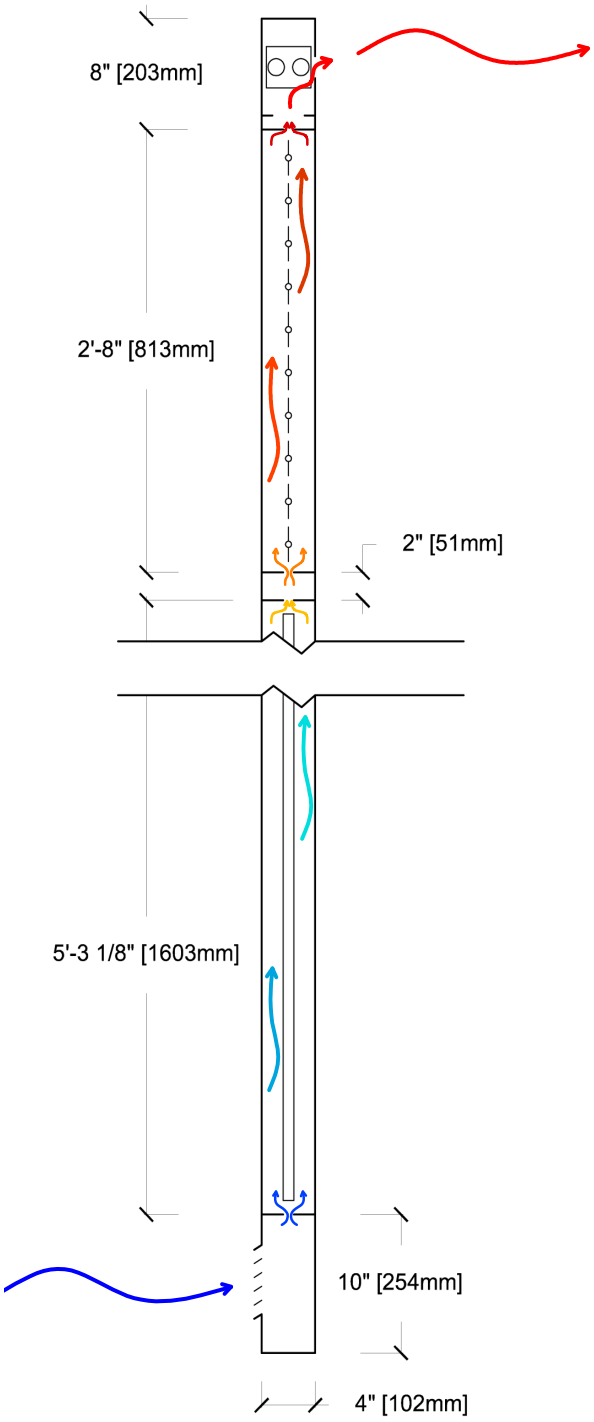

Fig 16: Cross section and airflow schematic.

Chapter 2

Measurement Instrumentation and Methods

2.1 Thermal Testing

Thermal measurements were taken in order to test the thermal performances of the prototype, which operates similarly to a solar air collector and therefore can be characterized using the same type of relationships, which will be discussed in the next section. The principal parameters of interest are the temperatures at the input and at the output of the window, the airflow properties, which includes the air velocity, air density and specific heat at constant pressure, and the solar radiation incident on the unit.

2 K-type (chromel-alumel) thermocouples were installed at the bottom vent (Fig 17) to sense the input temperature, and 4 K-type at the top vent for the output air tem-

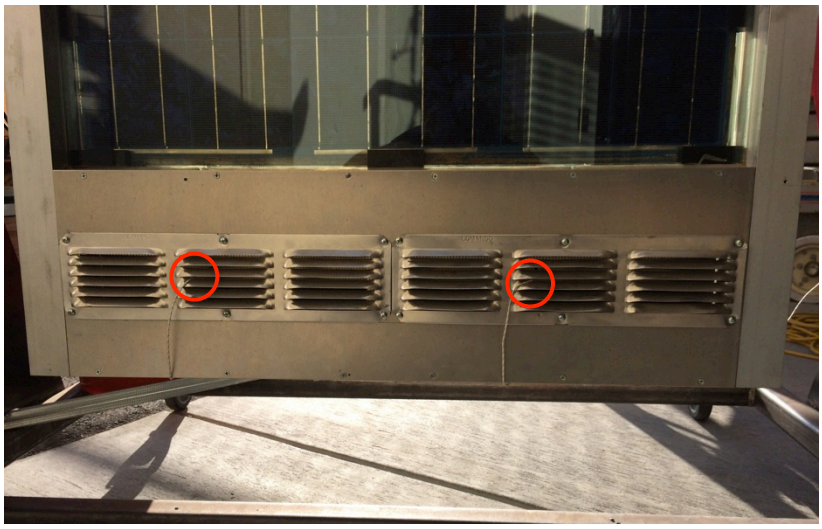

Fig 17: Thermocouples placement (marked with red circles) at the bottom vent.

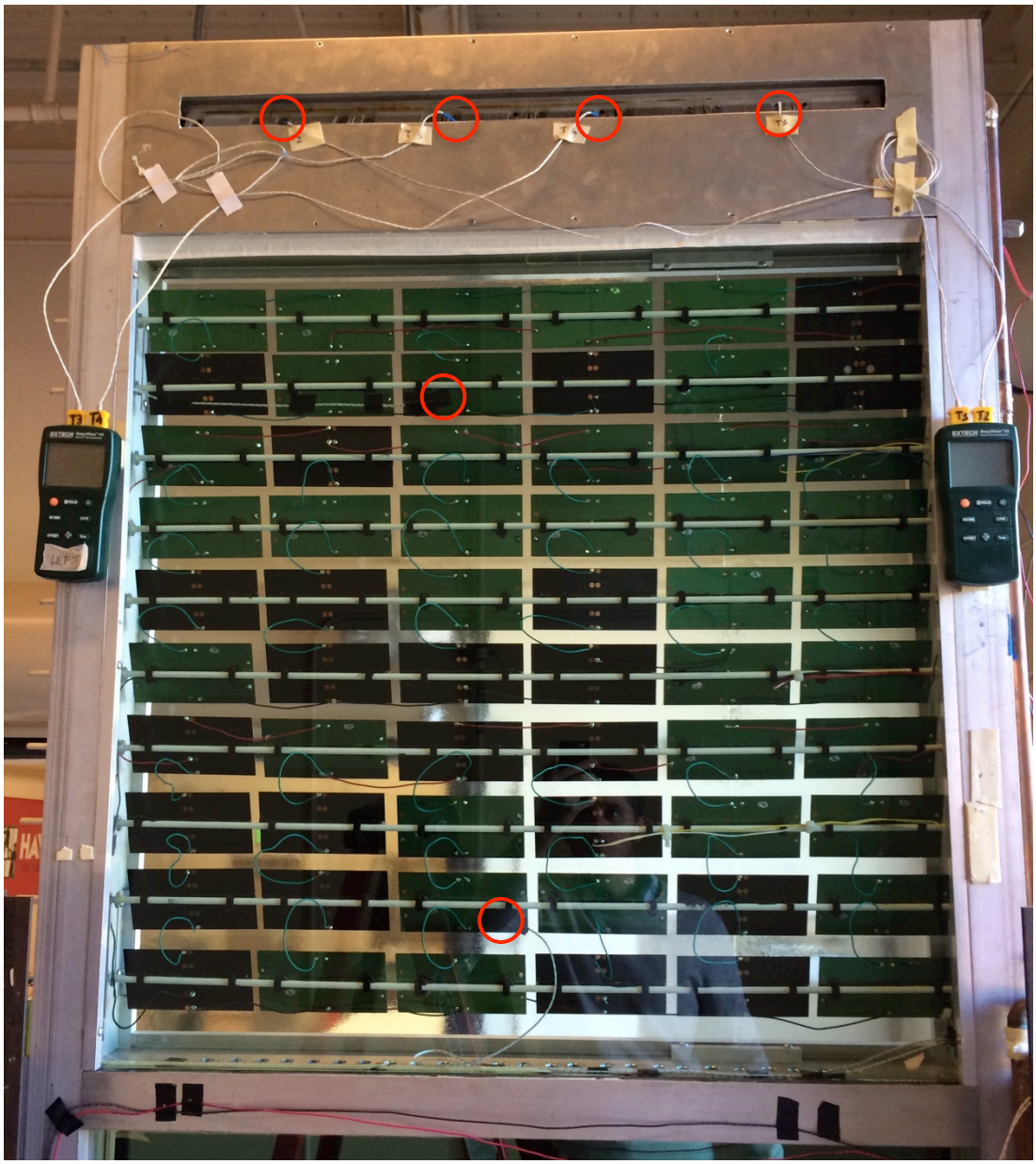

Fig 18: Thermocouples setup on the window back (red circles).

perature (Fig 18).

Two more thermocouples have also been installed on the back of two PV modules on the array, located one at the second row on the top and one at the second row from the bottom, in order to monitor the temperature levels reached by the array.

An Extech 410 Multimeter and two EA10 EasyView Dual Input Thermometers were used for reading and display of temperature data. The air velocity at the output has been tested with a Kanomax Anemomaster 6006 LITE hot wire anemometer (Fig 19), which reads the air speed in the direction perpendicular to the probe and has an accuracy of ±5%. To ensure this orthogonality condition, a small duct has been used to extend the output section and allow the air to come out horizontally. The measurements have been taken at nine different positions on the output section, and for each of them the probe was placed at three different height levels, so as to have a grid of 27 data points.

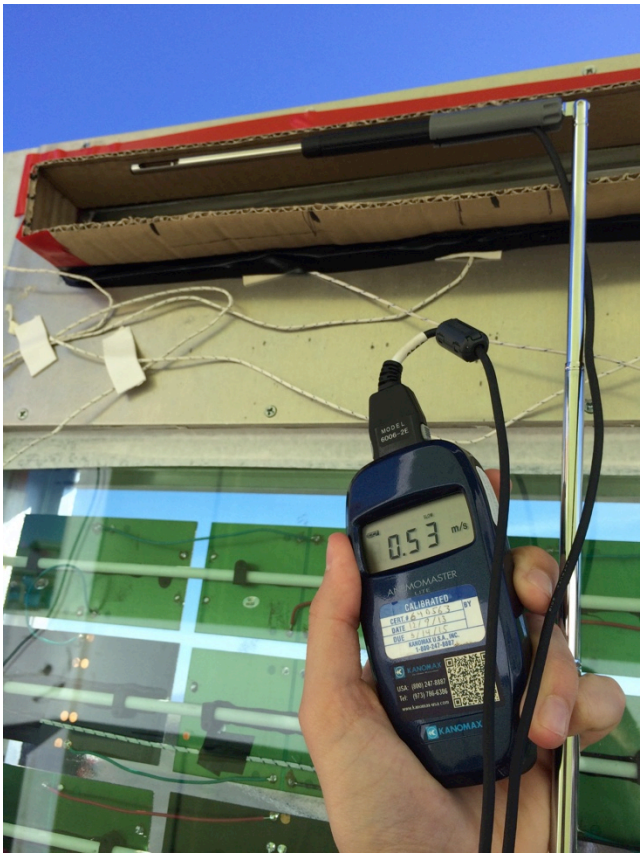

Fig 19: Hot wire anemometer for air velocity readings.

Table 2: Air velocity reading (in m/s) at 9 data points at different times.

		v_1	v_2	v_3	v_4	v_5	v_6	v_7	v_8	v_9
11:00	Top	0.26	0.75	0.98	1.18	1.1	1.1	1	1.15	0.92
	Middle	0.14	0.25	0.32	0.4	0.3	0.32	0.45	0.43	0.6
	Bottom	0.15	0.28	0.36	0.4	0.6	0.3	0.3	0.4	0.55
11.45	Top	0.24	0.7	1.08	1.05	1.15	1.15	1.08	1.25	0.8
	Middle	0.14	0.3	0.5	0.35	0.4	0.38	0.4	0.8	0.7
	Bottom	0.13	0.24	0.35	0.3	0.3	0.3	0.3	0.4	0.8
12:30	Top	0.35	0.64	1	1.1	1.2	1.15	1	1.2	1.25
	Middle	0.16	0.24	0.3	0.4	0.28	0.3	0.45	0.75	0.7
	Bottom	0.14	0.3	0.4	0.2	0.19	0.35	0.45	0.48	0.7

A sample of an air velocity data recording for 3 different times is reported in Table 2, where v_1, v_2, … v_9 represent the 9 evenly spaced data points, which go from left to right on the top vent cross section.

A pyranometer Ambient Weather TM-206, with an accuracy of ±10 W/m2, was used to record the global irradiance incident perpendicularly to the window surface, as well as the global tilted irradiance (including beam, diffuse and reflected components) at local solar azimuth and elevation.

2.2 Electrical Testing

The electrical generation of the top array, composed of the 60 PV modules, was tested. To compare the actual performances with the manufacturer's data, two PV modules were individually tested first, and their I-V characteristic curves were generated. These preliminary measurements were carried out by exposing the modules perpendicularly to the sun's rays and connecting them to a 350 Ω Ohmite RES350E-ND rheostat, which acts as a variable resistive load. By varying the rheostat resistance from 0 to 350 Ω, that is from a short-circuit to an almost open-circuit condition, the PV module response (in terms of voltage and current) has been recorded. The first module was tested outside the window, while the second was one of the modules on the bottom part of the array (3rd row from bottom), tilted by 20°, the latter receiving therefore less solar radiation due to reflective losses through the glass.

The electrical output of both modules is plotted in Fig 20, where the experimental data for current and power versus voltage are shown, along with their 6th order polynomial interpolation curves. The testing conditions and main data are reported in Table 3, where I_{PV} is the solar irradiance on the module's plane, T_{PV} is the temperature on the module's back, I_{sc} and V_{oc} are the short-circuit current and open-circuit voltage

Table 3: Testing conditions and data for I-V curve measurements.

	I_{PV}	T_{PV}	I_{sc}	V_{oc}	P_{max}
Outside module	1026 W/m^2	38 °C	190 mA	6.9 V	0.96 W
Inside module	920 W/m^2	49 °C	164 mA	6.4 V	0.78 W

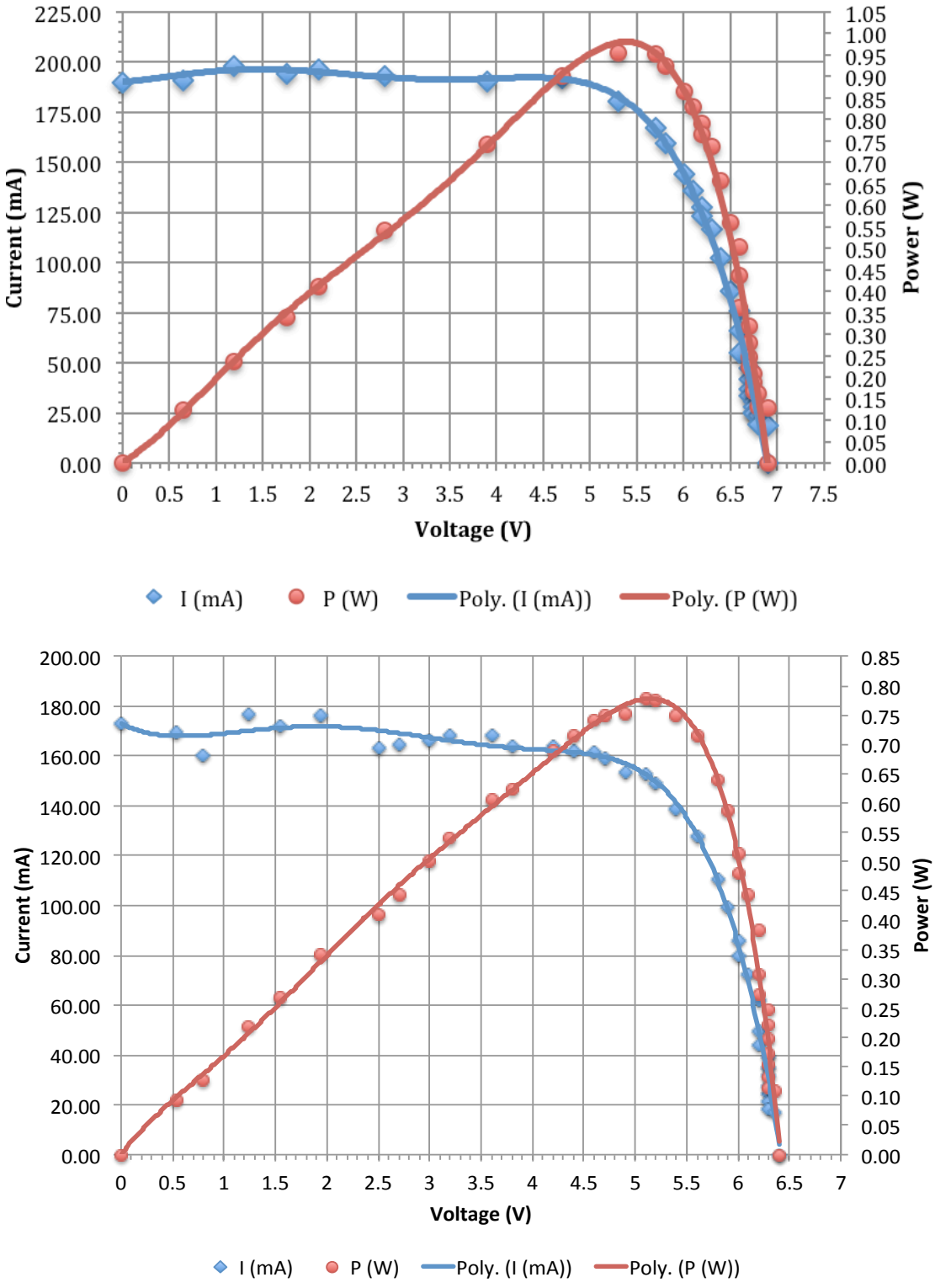

Fig 20: I-V characteristics for the PV module tested outside (top plot) and inside (bottom plot) of the double glazing.

recorded, respectively, and P_{max} is the maximum power produced.

It can be seen that the module tested outside behaves very closely to the manufacturer's specifications at standard testing condition (irradiance of 1000 W/m^2 and cell temperature of 25 °C), with a I_{sc} = 190 mA (vs. 183 mA at STC) and V_{oc} = 6.9 V (vs. 7.2 V at STC). The short-circuit current increase is caused by two factors that combine: the higher temperature of 38°C (even if current increases only slightly with temperature) and the higher solar irradiance of 1026 W/m^2. On the other hand, a higher irradiance causes a minimal increase in the voltage, while the higher temperature has a more significant impact in reducing it. The inside module receives instead a smaller amount of radiation (I_{PV} = 920 W/m^2), which causes a smaller short-circuit current (I_{sc} = 164 mA) and, due to the fact that is placed inside the double glazing, its temperature reaches a even higher value (T_{PV} = 49 °C), which results in a further reduction in open-circuit voltage, that drops to 6.4 V.

In the first case, a maximum power of 0.96 W has been obtained, which decreases to 0.78 W for the second module. These values can be used to calculate the temperature coefficient for power C_P, which indicates the power reduction per degree °C with respect to a reference situation, which can be calculated as follows [26]:

$$C_P = \frac{\Delta P}{\Delta T} = \frac{P' - P_{ref}}{T' - T_{ref}} \quad (1)$$

where P' and T' are the power and temperature at the actual measured conditions, that is P_{max} and T_{PV}, respectively, in this case, while P_{ref} and T_{ref} indicates instead the

same quantities calculated at a reference condition. The latter are considered to be the same as the power that a similar module at T_{ref} = 25 °C would generate with the same input solar irradiance. Under these conditions, the power P_{ref} is only dependent on the solar irradiance, and can be evaluated through the proportionality relation [27]:

$$\frac{P_{ref}}{P_{STC}} = \frac{I_{PV}}{I_{STC}} \tag{2}$$

with P_{STC} = 1 W and I_{STC} = 1000 W/m^2 are the power and current at standard testing conditions. For I_{PV} = 1026 W/m^2 (outside module), P_{ref} = 1.026 W, and for I_{PV} = 920 W/m^2 (inside module), P_{ref} = 0.92 W.

Therefore, by considering that P_{max} = 0.96 W and T_{PV} = 38°C, equation (1) gives in the first case a power temperature coefficient C_P = -0.00507 W/°C, while in the second case (for P_{max} = 0.78 W and T_{PV} = 49°C) it is C_P = -0.00583 W/°C, which is in line with the typical values found in commercial mono-crystalline Si modules, that is around -0.005 W/°C.

In order to measure the power output of the top PV array, consisting of the 60 modules, a stand-alone system was set up. The system was sized to be able to run a load P_{load} = 91 W, composed of the 10 DC fans, rated at 2.6 W each, and the 65 W water pump, for a period Δt = 5 hours continuously. The required energy E_{load} is then:

$$E_{load} = P_{load} \cdot \Delta t = 455 \text{ Wh} \tag{3}$$

By choosing a 12 V DC battery, the minimum capacity that it should provide is given by [27]:

$$C_{battery} = \frac{E_{load}}{V_{rated}} = 37.9 \text{ Ah} \quad (4)$$

where $C_{battery}$ is the battery capacity and V_{rated} is the rated battery voltage. A 40 Ah battery has been chosen. Generally a 12 V battery will have an actual voltage of 14 to 14.5 V, so in order to ensure that the array will effectively charge the battery the minimum array voltage needs to be corrected using the following relationship [27]:

$$V_{PV} = 1.2 \cdot \left\{ V_{rated} - \left[V_{rated} \cdot C_{\%V} \cdot \left(T_{\max} - T_{ref} \right) \right] \right\} \quad (5)$$

where V_{PV} is the array voltage, $C_{\%V}$ is the temperature coefficient for voltage, which is around -0.004 V/°C for most PV modules, T_{max} is the maximum expected module temperature and T_{ref} is the reference temperature, that is 25 °C. By using a rated voltage of 12 V and T_{max} = 60 °C, equation (5) gives a minimum voltage for the PV array of 16.4 V. An array voltage of 24 VDC was chosen, in order to minimize the current involved and then reduce power losses and the conductors' size. The 60 Parallax modules have been connected 4 by 4 in series, and the resulting 15 strings were parallel connected, as shown in Fig 21. The nominal voltage of the array is given by the rated module voltage (6 V) multiplied by the number of modules connected in series (4 in this case).

In order to determine the correct conductor size that is able to handle the actual operating currents, a maximum current should be evaluated. This would be the sum of the short-circuit current ratings of the parallel-connected modules (0.183 A x 15 strings)

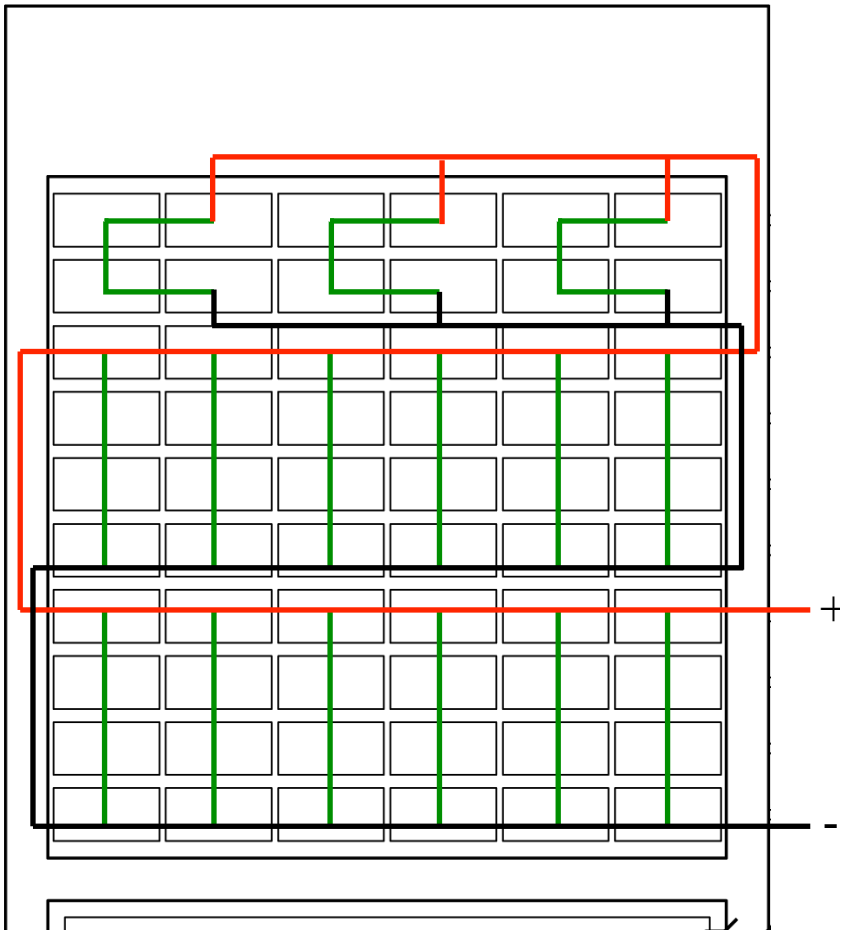

Fig 21: PV connection schematics: series connection (green) and parallel connections (red and black).

multiplied by a safety factor of 125%, which accounts for possible enhanced radiation levels that would produce higher currents, resulting in a maximum current of 3.43 A. For PV source circuits, as this is the case, an additional 1.25 factor is used to calculate the minimum ampacity (the current-carrying capacity) which the conductor should be sized for, that results in 4.29 A. Nominal ampacities for insulated conductors are generally based on an ambient temperature of 30 °C, and since the wires inside the air

cavities of the window will experience much higher temperature levels, a temperature correction factor is used to calculate the derated capacity [27]:

$$I_{nom} = \frac{I_{\max}}{C F_{temp}} \tag{6}$$

where I_{nom} is the derated conductor nominal capacity, I_{max} is the maximum circuit current previously calculated (4.29 A) and CF_{temp} is the temperature correction factor. The latter is given for various ambient temperature intervals in NEC Table 310.15(B)(2)(a), that is reported in Fig 22. By choosing a conductor with a USE-2 insulation with a 90°C rating, for a surrounding temperature above 60 °C, the CF_{temp}

TABLE 310.15(B)(2)(a) *Ambient Temperature Correction Factors Based on 30°C (86°F)*

For ambient temperatures other than 30°C (86°F), multiply the allowable ampacities specified in the ampacity tables by the appropriate correction factor shown below.

Ambient Temperature (°C)	Temperature Rating of Conductor			Ambient Temperature (°F)
	60°C	75°C	90°C	
10 or less	1.29	1.20	1.15	50 or less
11–15	1.22	1.15	1.12	51–59
16–20	1.15	1.11	1.08	60–68
21–25	1.08	1.05	1.04	69–77
26–30	1.00	1.00	1.00	78–86
31–35	0.91	0.94	0.96	87–95
36–40	0.82	0.88	0.91	96–104
41–45	0.71	0.82	0.87	105–113
46–50	0.58	0.75	0.82	114–122
51–55	0.41	0.67	0.76	123–131
56–60	—	0.58	0.71	132–140
61–65	—	0.47	0.65	141–149
66–70	—	0.33	0.58	150–158
71–75	—	—	0.50	159–167
76–80	—	—	0.41	168–176
81–85	—	—	0.29	177–185

Fig 22: Ambient temperature correction factors. Source: NEC Table 310.15(B)(2)(a).

ranges between 0.65 (for 61 - 65 °C) and 0.29 (for 81 - 85 °C). Since previous testings have reported temperature values for the PV array not exceeding 80 °C, a value of 0.41 for CF_{temp} has been selected, which through equation (6) gives I_{nom} = 10.46 A. The conductor size has been chosen to be 20 AWG (American Wire Gauge), which for conductors in free air has a rated ampacity of 13 A.

The complete PV system is composed of the 60 W rated PV array, the 40 Ah 12V DC battery and the 12V DC load represented by the fans, which have been all connected through a Tracer-2210RN MPPT solar charge controller, as shown in Fig 23. The

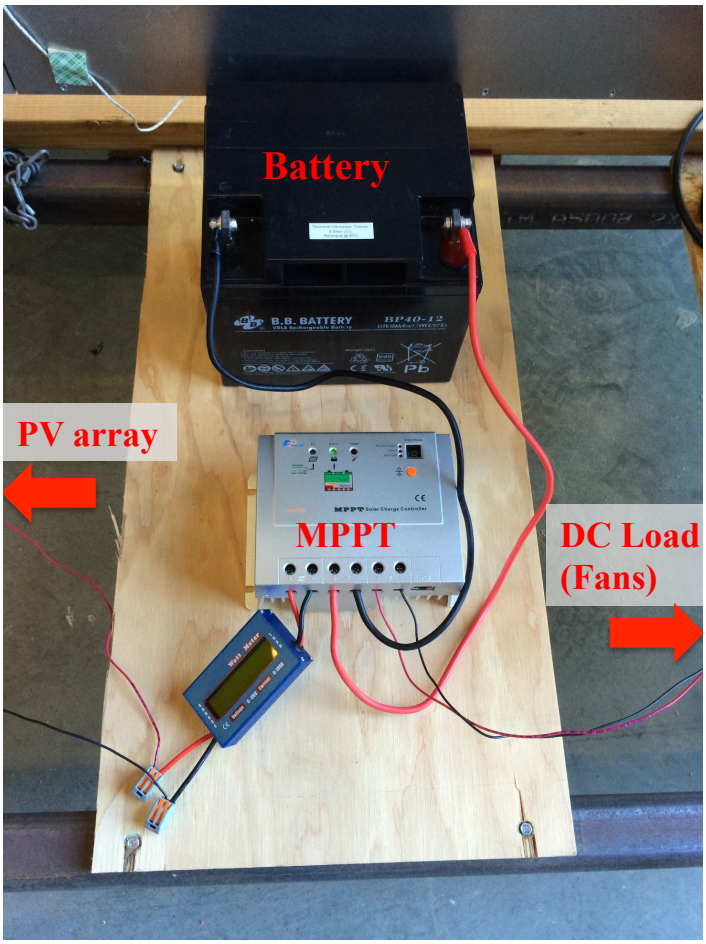

Fig 23: Photograph showing the charge controller, the battery and the connections with the PV array (left conductors) and DC fans (right conductors).

electrical specifications are reported in Table 4. This charge controller controls the charging voltage of the battery or the current supplied from the PV array, in order to allow the battery to operate at its maximum state of charge as well as to prevent any overcharge or overdischarge that will cause damages to the battery. Overcharge protection is realized by interrupting or limiting the current flowing from the array when the battery reaches a high state of charge (high voltage), while overdischarge protection involves the disconnection of the load when a low state of charge (low voltage) is detected.

A maximum power point tracking (MPPT) charge controller manages the power flow between the PV array and the loads, depending on the battery charge level, and ensures that the array works at the maximum power point it could achieve at any given time. The maximum power point tracking is realized, for any given set of temperature and irradiance conditions, by changing the resistance seen by the PV array, so that it is equal to the optimal load that corresponds to the maximum power point, that is [28]

Table 4: Charge controller specifications.

Model name	Tracer-2210RN
System Voltage	12 / 24 VDC
Rated Battery Current	20 A
Rated Load Current	20 A
Max PV input Voltage	100 VDC
Max PV input power	260 W (12 V system)
	520 W (24 V system)
Efficiency (for PV voltage = 24 V, PV power = 60 W and system voltage = 12 V)	95 %

$$R_{opt} = \frac{V_{MP}(T,I)}{I_{MP}(T,I)} \tag{7}$$

where R_{opt} is the optimal resistive load, and $V_{MP}(T, I)$ and $I_{MP}(T, I)$ are the maximum power voltage and current, which depend on temperature and irradiance. Fig 24 shows 3 different loads connected to a PV module at STC, corresponding to 3 different operating points on the I-V curve. When the load is equal to R_{opt}, the module operates at its maximum power point allowed by the external conditions, but if the load would change to $R_{LA} < R_{opt}$ (or $R_{LB} > R_{opt}$), the MPPT charge controller would increase (or decrease) the circuit resistance in order to bring the operating point back at, or close to MPP.

The DC input from the PV is converted to high frequency AC and rectified back

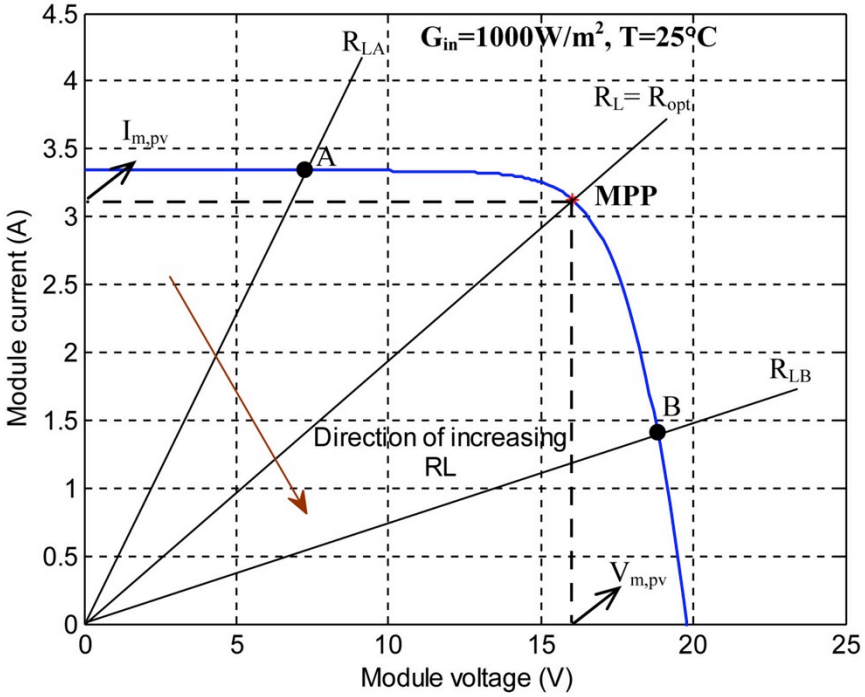

Fig 24: MPPT operation [28].

down to a different DC voltage and current, which match the battery. The voltage and current regulation follows the following relationship:

$$V_{out} \cdot I_{out} = \eta \cdot V_{in} \cdot I_{in} \tag{8}$$

where the subscripts *out* and *in* refer to the output and input voltage and current, respectively, and η is the charge controller efficiency. The charge controller converts the excess voltage from the PV array (most of the time greater than 12 V) down to a 12 VDC level, which is fed to the battery, while boosting the output current according to equation (8), with a 95% efficiency factor.

The PV array voltage, current and power output are measured by a wattmeter, which is placed between the array and the charge controller terminals. A remote display is also connected to the charge controller, indicating the voltage and current levels of both the battery and the load, as well as the battery capacity percentage (Fig 25).

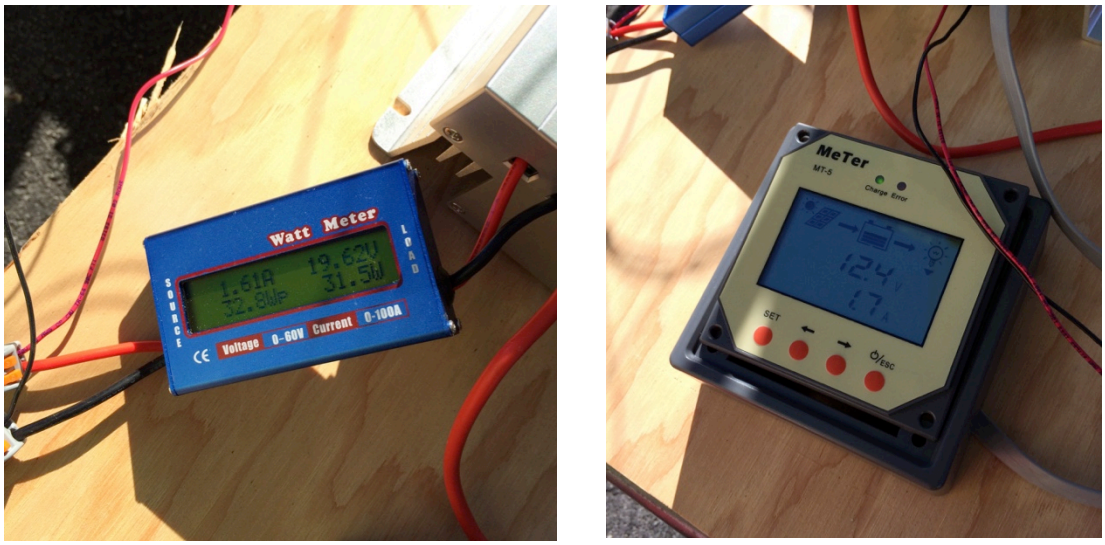

Fig 25: PV array, load and battery monitoring.

Chapter 3

Thermal And Electrical Performance Analysis

3.1 Thermal Output

The physical phenomena that take place when the prototype is fully operating involve all the three different types of heat transfer mechanisms, as well as a turbulent fluid flow due to the several obstacles the air encounters in its path through the unit (the input and output vents, the holes between the different sections and the PV modules). There is heat transfer by radiation between the sun and the exposed surfaces (resulting in a net heat absorption by the window), as well as radiation exchange between the different surfaces. Heat is then transferred inside by conduction from the exterior surfaces through the materials thickness, and there is convective heat transfer at the boundaries with the air, which removes the heat and carries it away in its ascending movement towards the top vent.

For the purpose of determining the prototype's thermal output, the complexity of this thermo-fluid dynamic problem can be reduced by treating the window as a black box, so that the output would include all previously mentioned effects.

Therefore, the system thermal performances has been computed based on the net heat transfer rate absorbed by the air and carried out of the window, which is considered a control volume with one inlet and one outlet, represented by the bottom and top vents. A one-dimensional flow approximation has been considered, which means that all the properties are uniform at any cross-section perpendicular to the fluid flow, that is

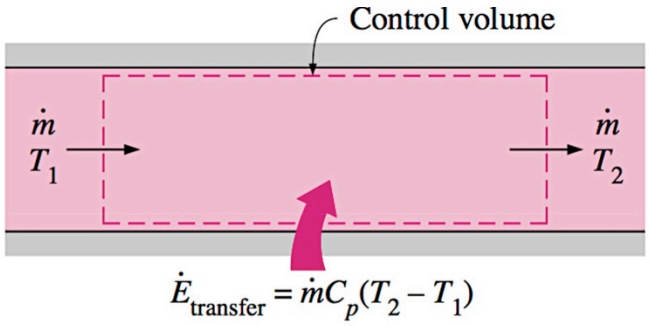

Fig 26: Energy transfer and mass flow rate conservation in a control volume in steady-state conditions [30].

generally true for flows in pipes or ducts. Moreover, all the variables (temperature, solar irradiance, air properties) are considered to vary only slowly during the course of the day, and then for each set of measurements the fluid flow can be well approximated as a steady-state system.

Under these conditions, the mass flow rate at the input of the control volume must be equal to that flowing out of it (Fig 26), and the net rate of heat transfer to the fluid $\dot{Q}$ [W] is given by [29]:

$$\dot{Q} = \dot{m} \cdot c_p \cdot \left(T_{out} - T_{in}\right) \tag{9}$$

where $\dot{m}$ [kg/s] is the mass flow rate, c_p [kJ/kg·K] is the air specific heat at constant pressure and $\Delta T = T_{\text{out}} - T_{\text{in}}$ [°C] is the temperature difference between the output temperature T_{out} and the input temperature T_{in}.

The specific heat of air between 20°C and 50°C, which is a common operating temperatures range for the window, does not change noticeably. It only varies from 1.005 kJ/kg·K at 300K to 1.007 kJ/kg·K at 330K, so the calculations have been made using an average constant value of 1.006 kJ/kg·K.

The mass flow rate $\dot{m}$ is calculated as follows [30]:

$$\dot{m} = \rho \cdot v \cdot A \tag{10}$$

where ρ [kg/m^3] is the air density, v [m/s] is the average air speed on a cross sectional area normal to the fluid flow, and A [m^2] is the area of the cross section. Since in steady-state the mass flow rate is constant at any cross-sectional area, $\dot{m}$ has been evaluated at the output vent, for which A is equal to 0.02484 m^2 and v is the velocity averaged over the measured values on the window outlet. The air density is computed for each set of data using the following relationship [30]:

$$\rho = \frac{p_a}{R_{air} \cdot T_{abs}} \tag{11}$$

where p_a [Pa] is the atmospheric pressure, R_{air} = 287.058 J/kg·K is the air gas constant, and T_{abs} [K] is the absolute temperature of the airflow.

In the estimation of the thermal efficiency, similarly to how efficiency is calculated for solar collectors, the thermal output is compared to the total solar power that the

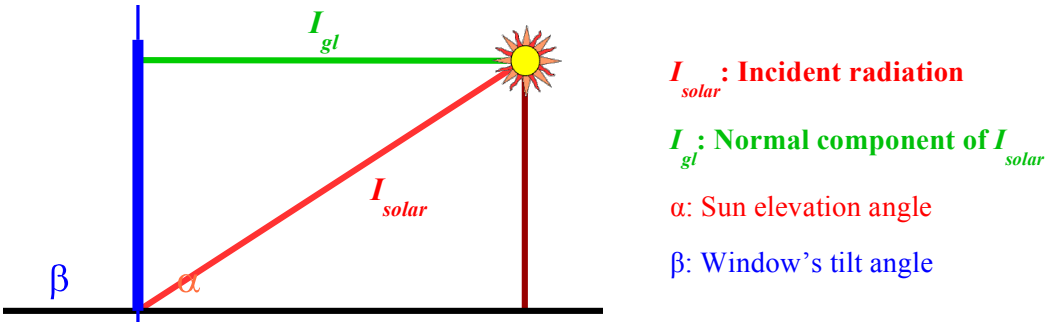

Fig 27: Incident and normal radiation on the window [31].

window receives, where only its component that is perpendicular to the window's plane has a useful effect, as illustrated in Fig 27. The thermal efficiency η_{th} can therefore be expressed as [10]:

$$\eta_{th} = \frac{\dot{Q}}{I_{gl} \cdot A_{gl}} \tag{12}$$

where I_{gl} [W/m^2] is the solar irradiance incident perpendicularly to the glass panels and A_{gl} [m^2] is the total frontal glazing area, equal to 1.958 m^2, which represents the useful effective area that captures and transfer the solar radiation to the PV absorbers. In Fig 28 is reported a sample of the worksheet table used for thermal measurements and computation of the required parameters for equations (9) – (12). I_panels represents the irradiance on the window's plane, while W_in is the total incident power, that is I_panels multiplied by the frontal glazing area A_{gl}, previously defined. The average of the two thermocouples readings at the bottom vent is also reported (T_In_Avg), along with the 4 temperature measurements at the top vent (T_1,…T_4) and their average T_out_Avg. The resulting average value V_Avg from the air velocity readings and the computed air density ρ are inputs for the calculation of the mass flow rate, here indicated as Γ. This, together with the derived temperature difference ΔT and the constant c_p, are used to calculate the thermal output and thermal efficiency (shown as Q and η).

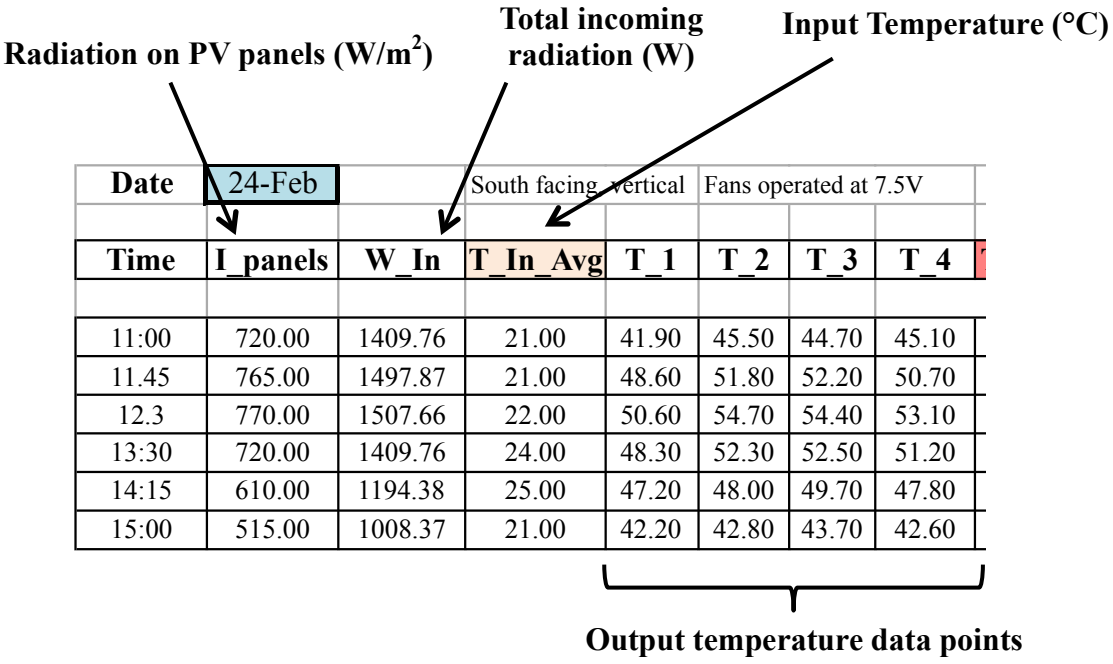

Date	24-Feb			South facing, vertical	Fans operated at 7.5V		
Time	I_panels	W_In	T_In_Avg	T_1	T_2	T_3	T_4
11:00	720.00	1409.76	21.00	41.90	45.50	44.70	45.10
11.45	765.00	1497.87	21.00	48.60	51.80	52.20	50.70
12.3	770.00	1507.66	22.00	50.60	54.70	54.40	53.10
13:30	720.00	1409.76	24.00	48.30	52.30	52.50	51.20
14:15	610.00	1194.38	25.00	47.20	48.00	49.70	47.80
15:00	515.00	1008.37	21.00	42.20	42.80	43.70	42.60

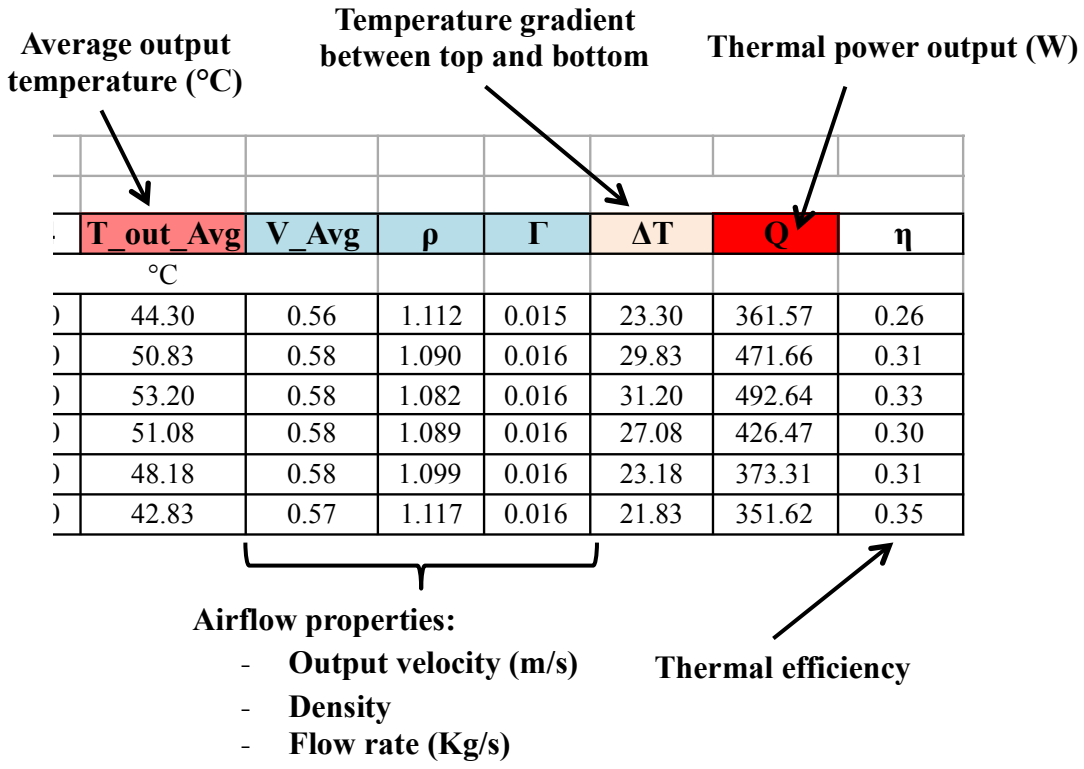

T_out_Avg	V_Avg	ρ	Γ	ΔT	Q	η
°C						
44.30	0.56	1.112	0.015	23.30	361.57	0.26
50.83	0.58	1.090	0.016	29.83	471.66	0.31
53.20	0.58	1.082	0.016	31.20	492.64	0.33
51.08	0.58	1.089	0.016	27.08	426.47	0.30
48.18	0.58	1.099	0.016	23.18	373.31	0.31
42.83	0.57	1.117	0.016	21.83	351.62	0.35

Fig 28: Example of thermal measurements data worksheet and parameters computation.

3.2 Electrical Output

The PV system described in the previous chapter was used to monitor the photovoltaic array output and evaluate the electrical generation efficiency at which the system is able to operate.

The specifications for the installed Parallax modules, which were given in Fig 14, can be used to calculate the rated electrical efficiency at STC, as well as the fill factor (FF). The latter is defined as the ratio of maximum power (equal to the product of maximum power voltage and current) to the product of open-circuit voltage and short-circuit current, and represents the squareness of the I-V characteristic and is a measure of the quality of a photovoltaic device. High fill factor values indicate a low equivalent series resistance and a high equivalent shunt resistance, which implies that less current is dissipated in internal losses. In terms of the I-V characteristic this means that in solar cells with a high FF the maximum power voltage and current are

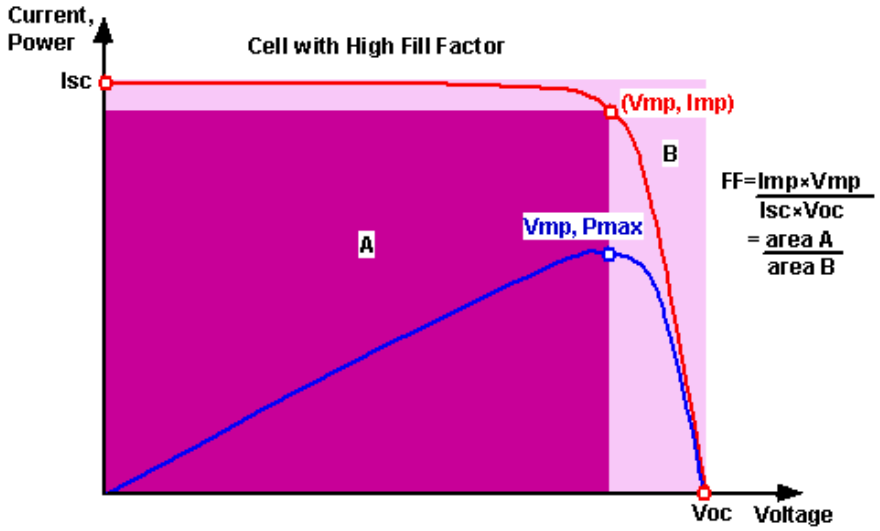

Fig 29: Fill factor representation on the I-V curve [31].

closer to the open-circuit and short-circuit current, respectively, as shown in Fig 29. Commercial solar cells have generally a fill factor > 70%, while the maximum value for Si is around 0.83. The fill factor FF for the Parallax modules has been determined to be [32]:

$$FF = \frac{V_{MP} \cdot I_{MP}}{V_{OC} \cdot I_{SC}} = 0.756 \tag{13}$$

where V_{MP} = 6 V, I_{MP} = 0.166 A, V_{OC} = 7.2 V and I_{SC} = 0.183 A are the voltage and current at maximum power point and the open-circuit voltage and short-circuit current, respectively.

The rated electrical efficiency of a single module $\eta_{el,\ rated}$ at standard testing conditions (AM=1.5, 25°C and 1000 W/m^2) is given by [33]:

$$\eta_{el,\ rated} = \frac{V_{OC} \cdot I_{SC} \cdot FF}{I_{solar} \cdot A_{panel}} = 12.65\% \tag{14}$$

where I_{solar} is the solar irradiance, equal to1000 W/m^2, and A_{panel} is the area of a single PV panel of 7.87 x 10^{-3} m^2.

The actual operating efficiency of the array, which takes into account the effect of a lower solar irradiance (due to the modules' tilting, ambient variations though the day and reflection and transmission losses through the glazing) and a higher operating temperature, can be instead evaluated similarly to equation (12) as follows [27]:

$$\eta_{el} = \frac{P_{el}}{I_{gl} \cdot A_{PV}} \tag{15}$$

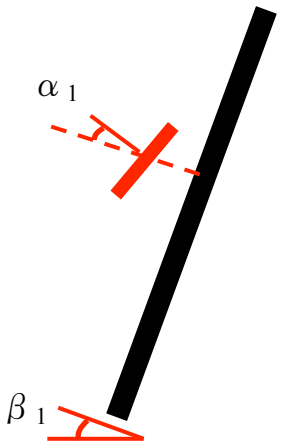

Fig 30: Schematic showing the tilting angles for the prototype (black) and PV array (red).

where A_{PV} is the total area of the 60 PV modules, which is equal to 0.4725m^2, and P_{el} is the observed electrical power output.

An example of the worksheet used for the electrical testing is shown in Fig 31. Here β_1 represents the tilting angle of the normal to the window with respect to the ground, while α_1 is the angle of the PV array with respect to the window's plane, as shown in Fig 30 (therefore, a situation with both β_1 and α_1 equal to 20° refers to a 40° total tilting of the array with respect to ground). On the table the voltage and current levels for the PV array, the battery and the DC fans are also reported, along with the generated power and the solar irradiance in the direction of the normal to the modules surface (I_panels). The last two columns are instead the temperature reading of the two thermocouples installed on the back of the PV modules, one on the top part and one on the bottom part of the array.

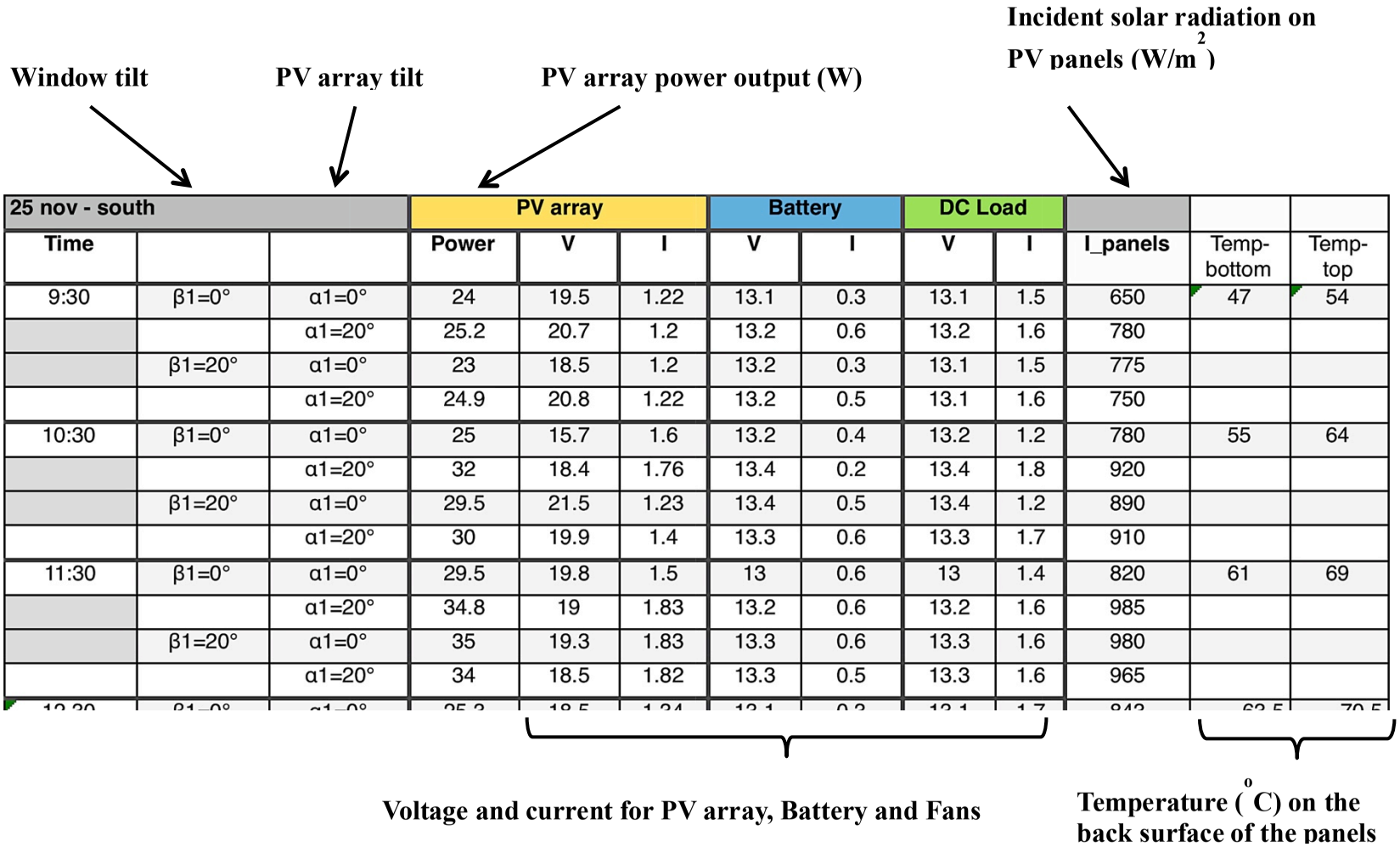

25 nov - south			PV array			Battery		DC Load				
Time			Power	V	I	V	I	V	I	I_panels	Temp-bottom	Temp-top
9:30	β1=0°	α1=0°	24	19.5	1.22	13.1	0.3	13.1	1.5	650	47	54
		α1=20°	25.2	20.7	1.2	13.2	0.6	13.2	1.6	780		
	β1=20°	α1=0°	23	18.5	1.2	13.2	0.3	13.1	1.5	775		
		α1=20°	24.9	20.8	1.22	13.2	0.5	13.1	1.6	750		
10:30	β1=0°	α1=0°	25	15.7	1.6	13.2	0.4	13.2	1.2	780	55	64
		α1=20°	32	18.4	1.76	13.4	0.2	13.4	1.8	920		
	β1=20°	α1=0°	29.5	21.5	1.23	13.4	0.5	13.4	1.2	890		
		α1=20°	30	19.9	1.4	13.3	0.6	13.3	1.7	910		
11:30	β1=0°	α1=0°	29.5	19.8	1.5	13	0.6	13	1.4	820	61	69
		α1=20°	34.8	19	1.83	13.2	0.6	13.2	1.6	985		
	β1=20°	α1=0°	35	19.3	1.83	13.3	0.6	13.3	1.6	980		
		α1=20°	34	18.5	1.82	13.3	0.5	13.3	1.6	965		
12:30	β1=0°	α1=0°	25.3	18.5	1.84	13.1	0.3	13.1	1.7	843	63.5	70.5

Fig 31: Example of electrical testing.

Chapter 4

Results And Discussion

4.1 Summer Measurements

Measurements on the thermal system were performed in Salinas, CA, in mid July, under 4 different conditions. The window was tested in an outside environment in both south-facing position and in sun tracking mode, with the latter meaning a continuous change of orientation of the prototype during the course of the day in order to keep it directed towards the sun. In both configurations, the window has been operated at 90° and 70° tilt angle with respect to the ground, corresponding to the window

Fig 32: Tilting of the prototype by 20°.

in vertical position and tilted by 20°, respectively. A picture of the window in 20° tilting position is shown in Fig 32.

After the first testing trials, the weather conditions characterized by growing wind during the afternoons coming from West and North-West suggested a different location for the prototype, since it was observed that this affected both the temperature and air velocity readings, due to the cooling action of the wind on the sensors and the added turbulence on the back of the unit. The window was then moved close to the south wall of a pocket house (Fig 33), built on the same location, in order to provide

Fig 33: Location for outside measurements.

shielding from the wind and ensure more stable conditions for taking data at the back of the prototype.

The results for the normal solar irradiance incident on the window plane and output air temperature the are shown in Fig 34, while those for the air temperature rise between the output and input vents and the heat transfer rate are reported in Fig 35.

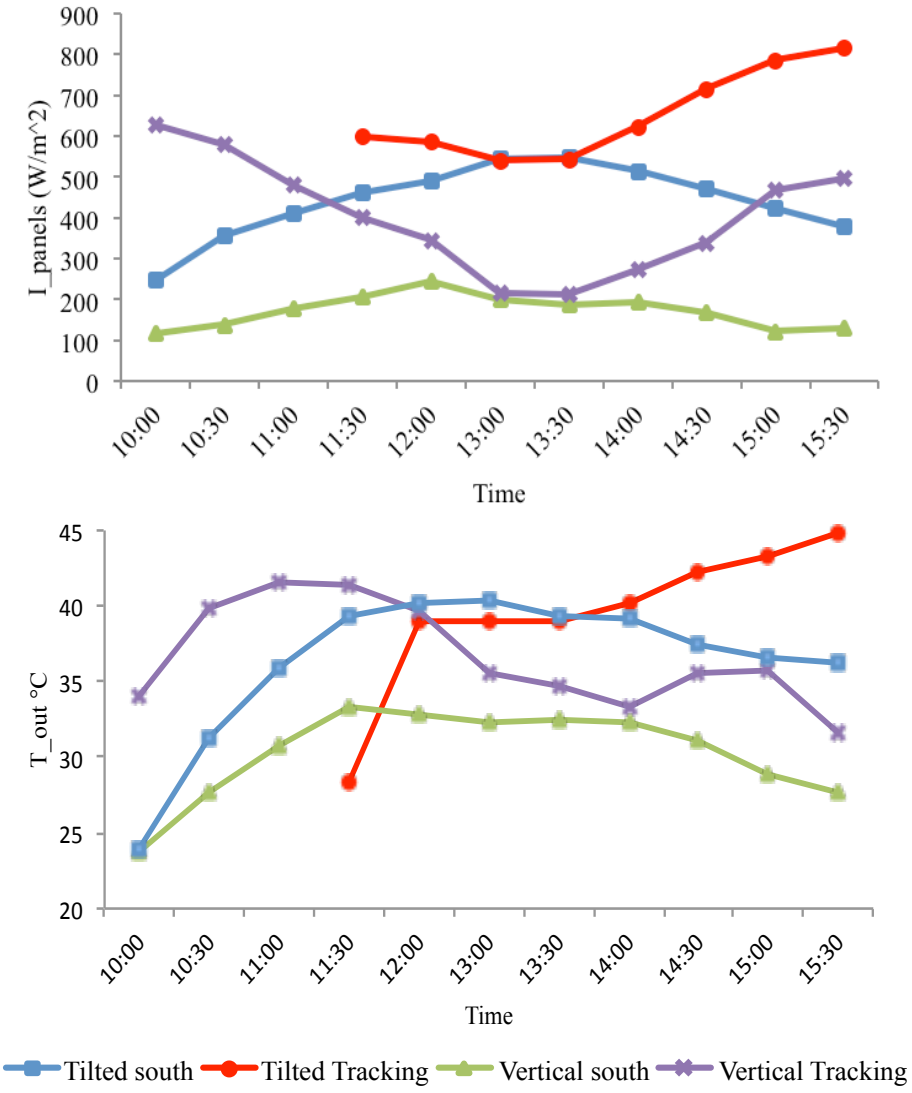

Fig 34: Normal irradiance (top) and output temperature (bottom) for summer measurements.

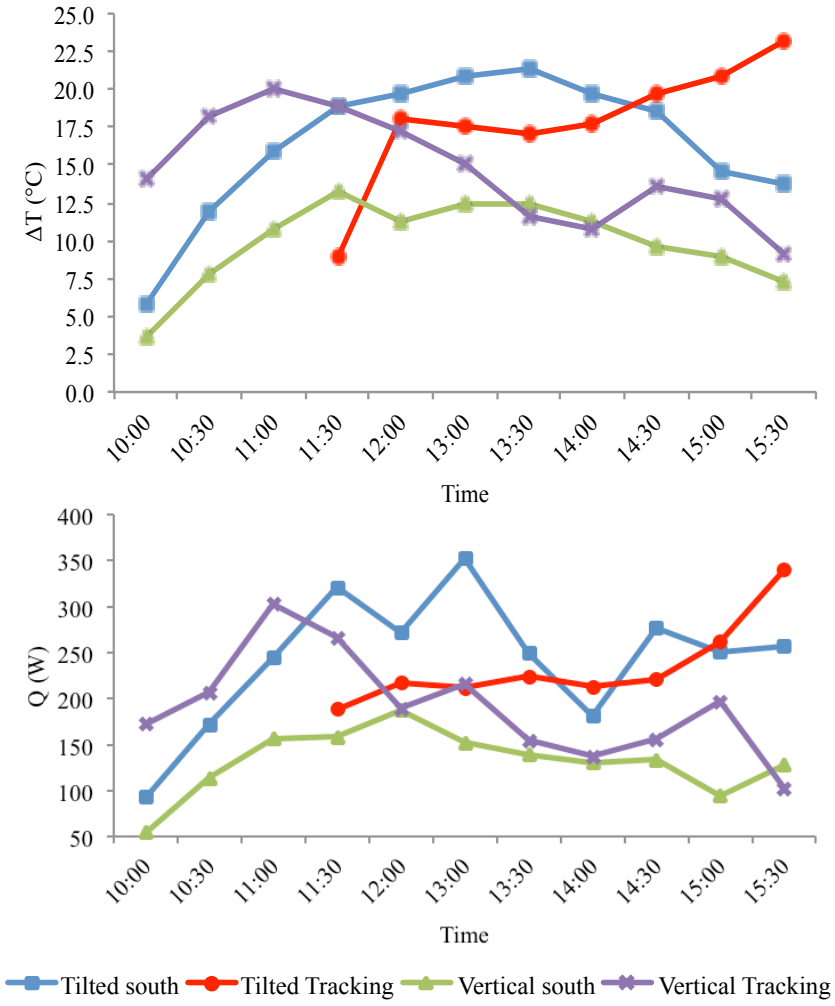

Fig 35: Temperature rise (top) and heat transfer rate (bottom).

It can be noticed that by keeping the window oriented south, a tilt angle of 20° almost doubles the performances, with respect to the vertical position situation. The average temperature difference between 11:00 and 14:30 increases from 10 °C in vertical position to around 20 °C in tilted position, and as a result the heat transfer rate rises from an average of 150 W to almost 300 W. The maximum output temperature of the

air increases as well from about 32 °C to slightly more than 40 °C, with a starting temperature of about 20 °C in both situations.

Looking at the solar irradiance profiles, it appears that the better tilting affects the radiation captured, so that the tilted south-facing configuration has the same shape of the vertical south-facing one, but it is shifted up towards higher irradiance values. At 10:00, for example, the normal irradiance is about 100 W/m^2 in the vertical case, and around 250 W/m^2 in the tilted case, and at noon is about 200 and 500 W/m^2, respectively. Therefore, a tilting of 20° increases the incident radiation by a factor of about 2.5.

In the ideal scenario of a window always oriented in the direction of the sun, in what has been called a tracking mode, the radiation capture is further increased in morning and afternoon hours, where the elevation angle of the sun is lower, causing a bigger portion of the radiation normal component to reach the window surface. In a similar way, the performances of the tracking configurations with respect to the relative fixed south-facing counterparts are very close in the middle of the day, and much higher in earlier and later hours. As a comparison, the output temperature in tilted tracking mode maintains close to the tilted south-facing configuration (around 40 °C), and increases up to 45 °C in the afternoon. The ΔT and the heat transfer rate are instead slightly below in the central hours with respect to the fixed tilting case, even though this might be due to a different ambient temperature, as well as to a different wind speed, which affected both the cooling rate of the window and the top vent airflow measurements (resulting in an oscillating thermal power output).

4.2 Fall Measurements

Other measurements were taken in November and both the thermal and the electrical performances have been tested. Two sets of measurements were taken: the first set of data has been taken with the window tracking the sun during the day, and the second with the window in fixed south-facing position.

In both cases, the window was maintained vertical at an angle of 90° (with respect to the ground) for the whole day, and only during PV power measurements the tilt angles of both the window and the PV modules were changed, so as to have 4 different tilting conditions for each time data point and compare the different outputs that the array was able to produce at the same moment. By defining β_1 as the angle between the normal to the window and the ground, and α_1 as the angle between the normal to the PV modules and the window's normal (Fig 36), each PV measurement has been done by changing the tilting conditions sequentially as follows:

- $\beta_1 = 0°$, $\alpha_1 = 0°$;
- $\beta_1 = 0°$, $\alpha_1 = 20°$;
- $\beta_1 = 20°$, $\alpha_1 = 0°$;
- $\beta_1 = 20°$, $\alpha_1 = 20°$.

The results for the thermal measurements are shown in Fig 37. Because of the lower elevation angle of the sun with respect to the summer testing, which resulted in a smaller radiation component reaching the collector horizontally, in fall the thermal performances in vertical position are better than the ones obtained with a 20° tilting in

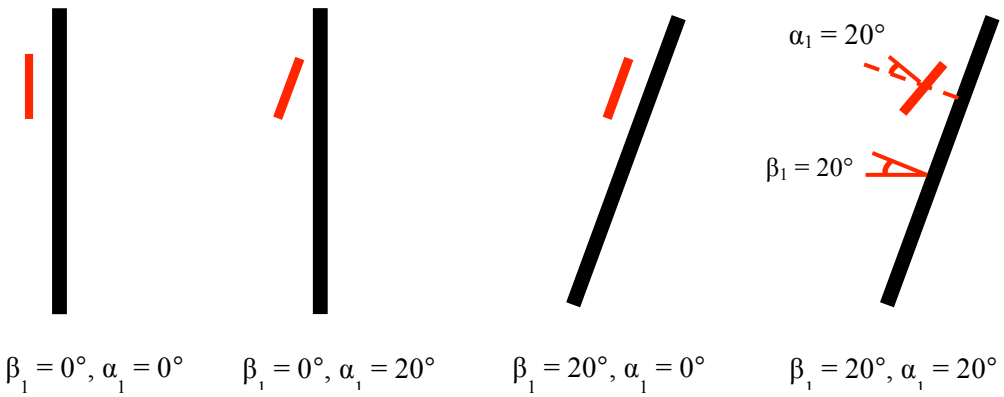

Fig 36: Schematics of the 4 different tilting conditions.

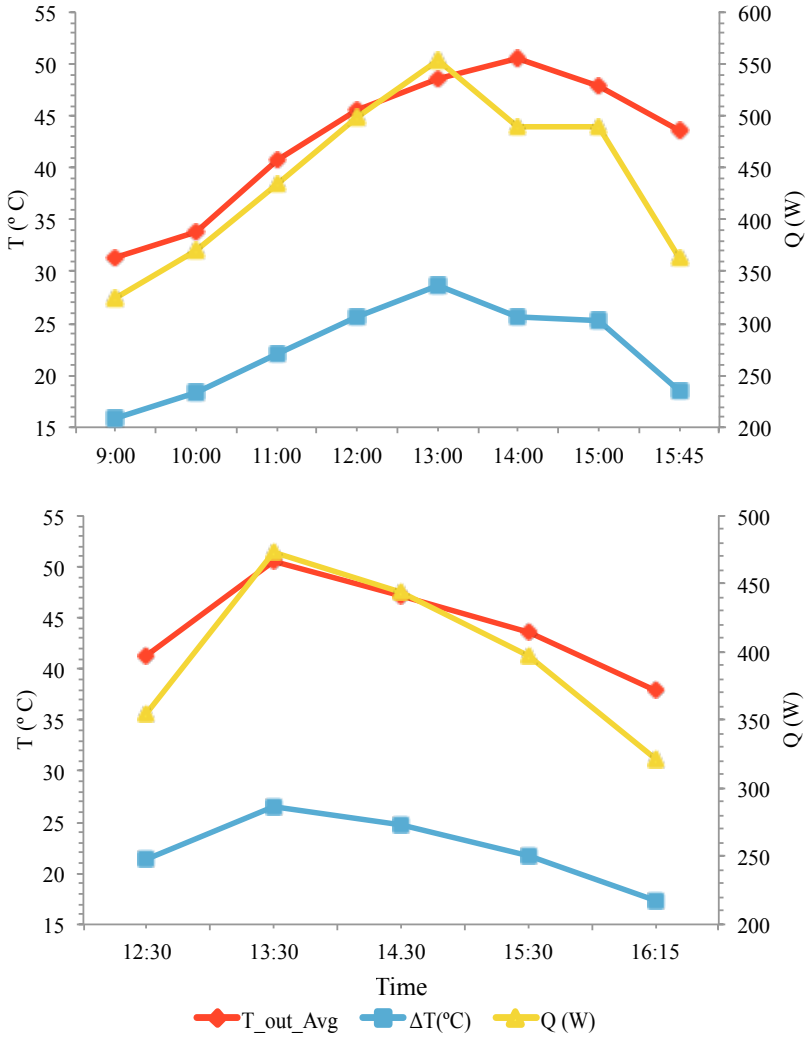

Fig 37: Performance testing in fall: temperature, thermal power output and temperature difference for the south-facing (top) and tracking (bottom) conditions.

July, with an average ΔT of about 22 °C in both tracking and south-facing positions, and an average heat transfer rate of 400-450 W. The air at the outlet reached 50 °C in both cases, with an average of around 43-44 °C.

The testing on the photovoltaic system (Fig 38) shows minimal differences in the power output. In the south-facing scenario the worst configuration is represented by the window vertical with the PV array parallel to the window's plane ($\beta_1 = 0°$, $\alpha_1 = 0°$), which gives an average power of 23 W, with a peak of 29.5 W. The other configurations are instead very close, with average powers between 24.5 and 25.5 W and a peak of 34-35 W.

In tracking mode it is the most tilted configuration ($\beta_1 = 20°$, $\alpha_1 = 20°$) whose performance is the poorest with respect to the others, with a peak of 36 W and an average of 29.7 W. This is due to the fact that the PV modules received less radiation in early morning and late afternoon hours, because of the high tilting (40° in total) and low elevation of the sun. Previous configurations have instead a very similar behavior, with averages of 31.5-32 W and peaks of 37-37.5 W.

The high temperature levels, to which the PV modules are subjected, ranging from 55 to 70 °C, is one of the main causes of electrical efficiency losses. Considering the south-facing situation with $\beta_1 = 0°$, $\alpha_1 = 0°$ as an example, the peak in power is 29.5 W at 11:30, when the modules average temperature is 65 °C. The measured irradiance normal to the array plane at that time is 820 W/m2, which results in a total input power on the whole array of 387.45 W. The actual operating efficiency can then be calculated by the ratio of power generated to the input power, which is equal to

(29.5 / 387.45) x 100 = 7.6%, a result that includes optical losses through the glass, thermal losses due to the high operating modules temperatures, as well as system losses such as mismatch losses between the 60 PV modules, transmission losses through the conductors, and electronic converter losses (MPPT).

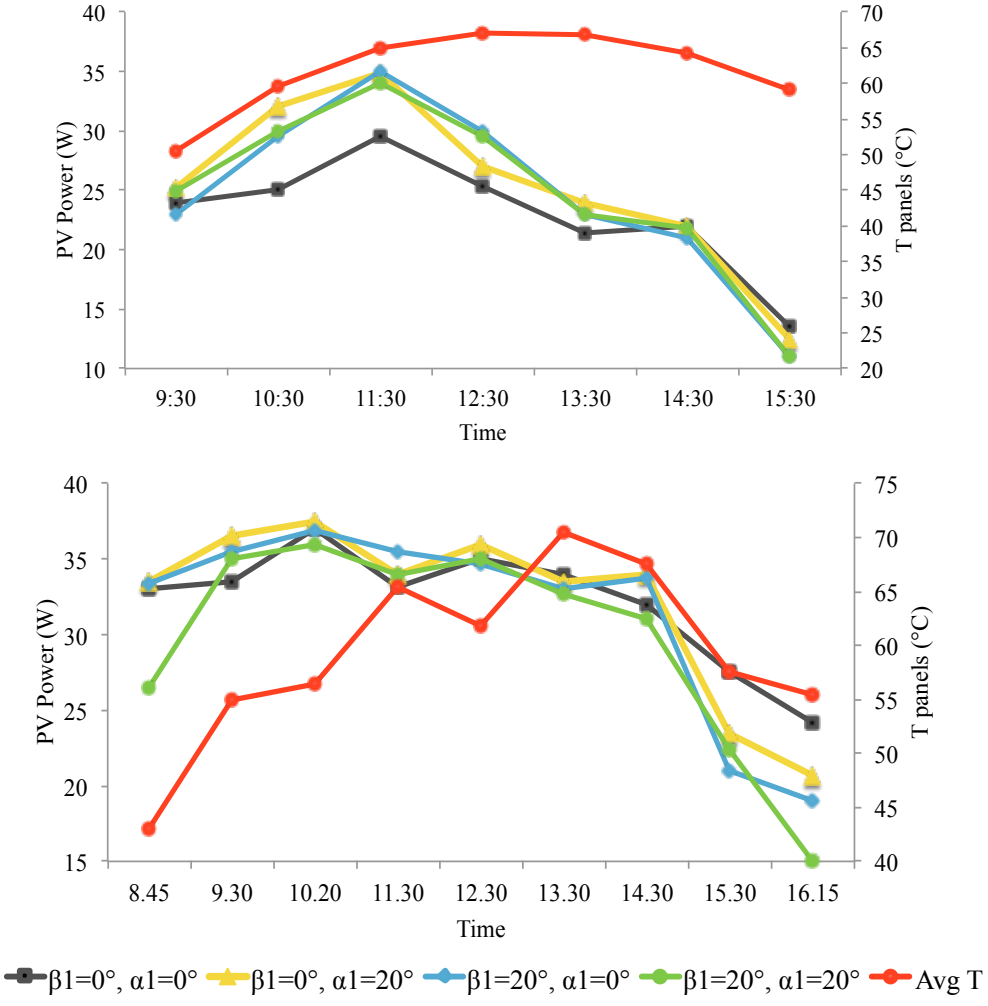

Fig 38: PV array power output and temperature in different tilting conditions, for the south-facing (top) and tracking (bottom) cases.

4.3 Winter Measurements

Other measurements were taken in February on both the thermal and the electrical system, and the impact of the airflow on the overall performances has been examined. The window was tested in vertical south-facing position, with the PV array at 90°- tilt angle, relative to the ground.

The voltage of the fans was tuned to obtain four different voltage levels. These are 6 V, 7.5 V, 9 V and 12 V, and the corresponding average air speeds measured at the output vent are, respectively, 0.5 m/s, 0.58 m/s, 0.64 m/s and 0.8 m/s, showing a linear increase of the air velocity with the voltage (Fig 39).

The results for the four configurations are shown in Fig 40, while the average values for the temperature rise ΔT, the electrical power P_{el}, the heat transfer rate Q, the input and output air temperature T_{in} and T_{out}, and the power consumption of the fans are reported in Table 5. It can be noticed that lower air speed values result in higher temperature rises, which are close to 26°C for the 6 and 7.5 V cases, but also in lower

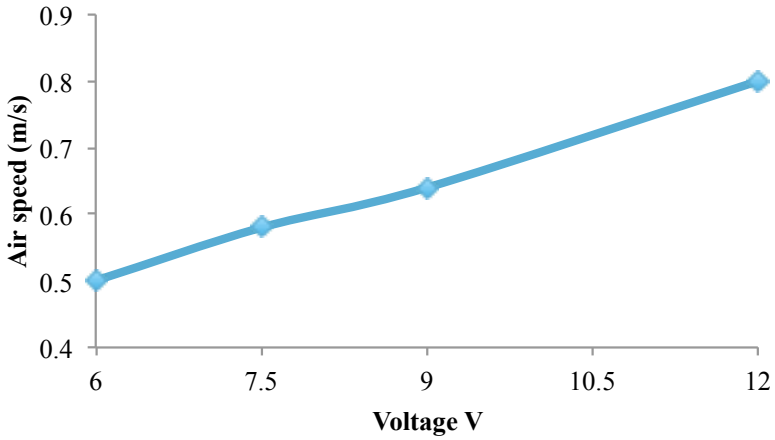

Fig 39: Air velocity increment with the fans voltage.

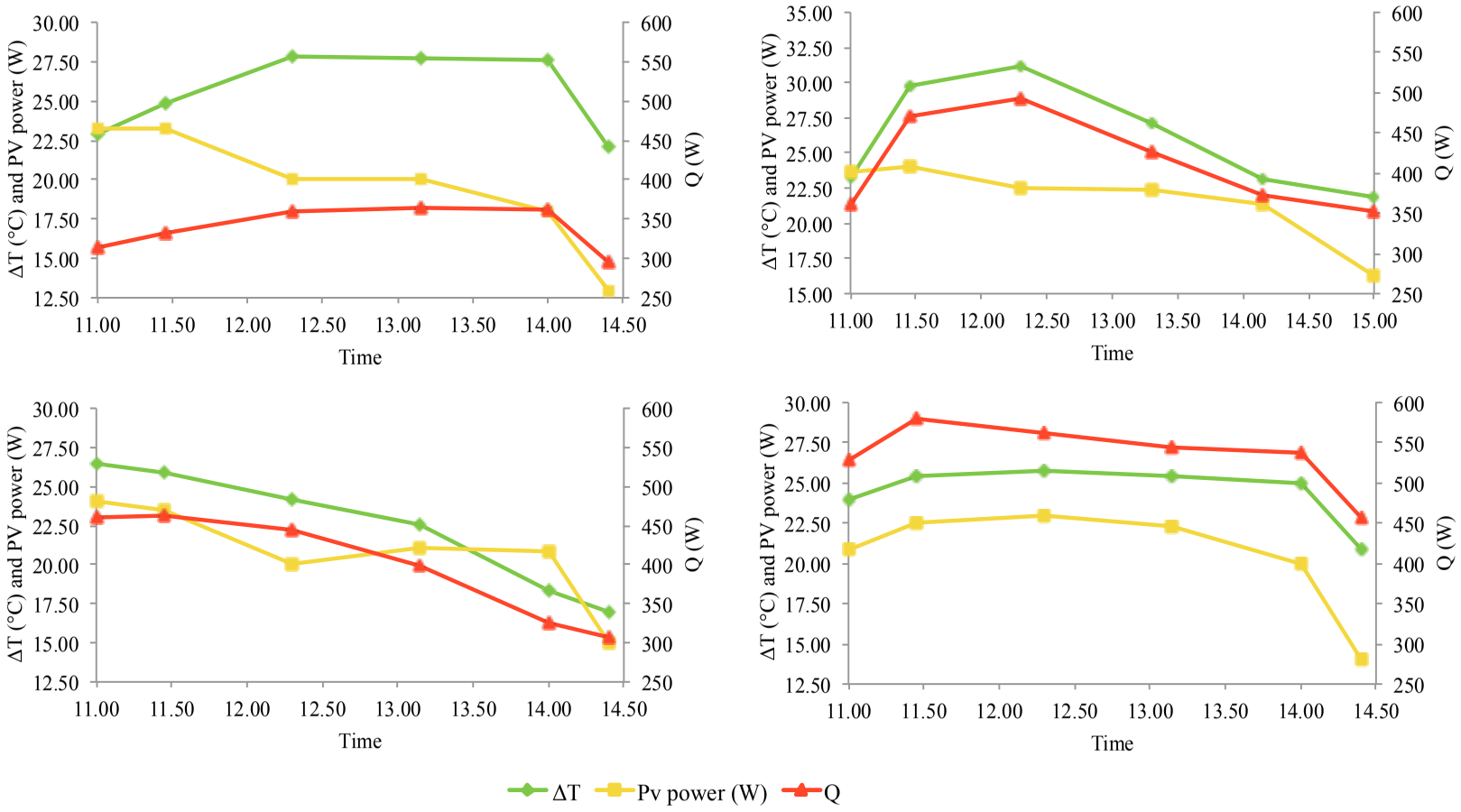

Fig 40: Temperature difference, electrical and thermal power output for different voltage levels: 6V (top left), 7.5V (top right), 9V (bottom left) and 12V (bottom right).

thermal outputs, equal to 340 and 413 W, respectively. This is due to a lower convective heat transfer coefficient between the absorber surfaces (the PV modules) and the air, which results in lower heat transferred to the air and higher surface temperatures. At the highest voltage level of 12 V, corresponding to an air speed of 0.8 m/s, the ΔT drops to 24.4°C, but the heat transfer rate absorbed by the air rises to 535 W.

The electrical generation is not affected too much by the airflow, and the average is close to the 20-21 W range in all situations, while the power consumption of the fans is maximum (19.5 W) at the rated voltage of 12 V and is less than half of this value for lower voltages.

Therefore, if thermal energy at lower temperature can be used, a higher mass flow rate is recommended, as it would improve the heat generated and the system thermal efficiency, even though the increased electrical demand for ventilation should be considered as well. For applications with a higher temperature requirement, such as space heating, a lower mass flow rate can be used, so that an air velocity of 0.58 m/s represents the optimal configuration, as it provides the highest temperature rise, and a rela-

Table 5: Average parameters under different voltage configurations: Air speed, temperature difference, electrical and thermal powers, input and output temperatures and power consumed by the fans.

Fans voltage (V)	Air speed (m/s)	ΔT (°C)	P_{el} (W)	Q (W)	T_{in} (°C)	T_{out} (°C)	Fans power consumption (W)
6	0.5	25.5	19.6	340	27.4	52.9	5
7.5	0.58	26	21.7	413	22.3	48.4	8.25
9	0.64	22.4	20.7	400	20	42.3	10.5
12	0.8	24.4	20.4	535	22.8	47.2	19.5

tively high heat transfer rate, as well as low power consumption by the fans, equal to only 8 W, resulting in a positive net electrical generation.

The thermal and electrical efficiency of the window under the different airflow conditions are reported in Fig 41. As the airflow rate increases, the thermal efficiency increases as well, since a greater volume is in contact with the PV array, therefore enhancing the heat transfer coefficient between the modules and the air, which results in more heat generated for the same incident solar radiation. A smaller temperature difference with respect to the ambient temperature also contributes to higher efficiencies at higher flow rates, because of the smaller heat losses that this implies, while at lower airflows the higher temperatures produce higher convective and radiative losses to the environment.

The values of thermal efficiency ranges between 23 - 31 % for 6 V, 26 - 35 % for 7.5 V, 26 - 33 % for 9 V and 40 - 44 % for 12 V, with average values of 27 %, 31 %, 30 % and 42 %, respectively. The optimal airflow for the temperature rise then results in a thermal efficiency in the 31% range, while if efficiency and heat absorbed are required to be maximized, higher airflows hold better results, with an efficiency of 42%. The electrical efficiency is instead very close in both situations, and ranges between 6 and 7%, with a flatter profile for the 12V case, due to the lower temperature and higher cooling action on the PV modules by the air.

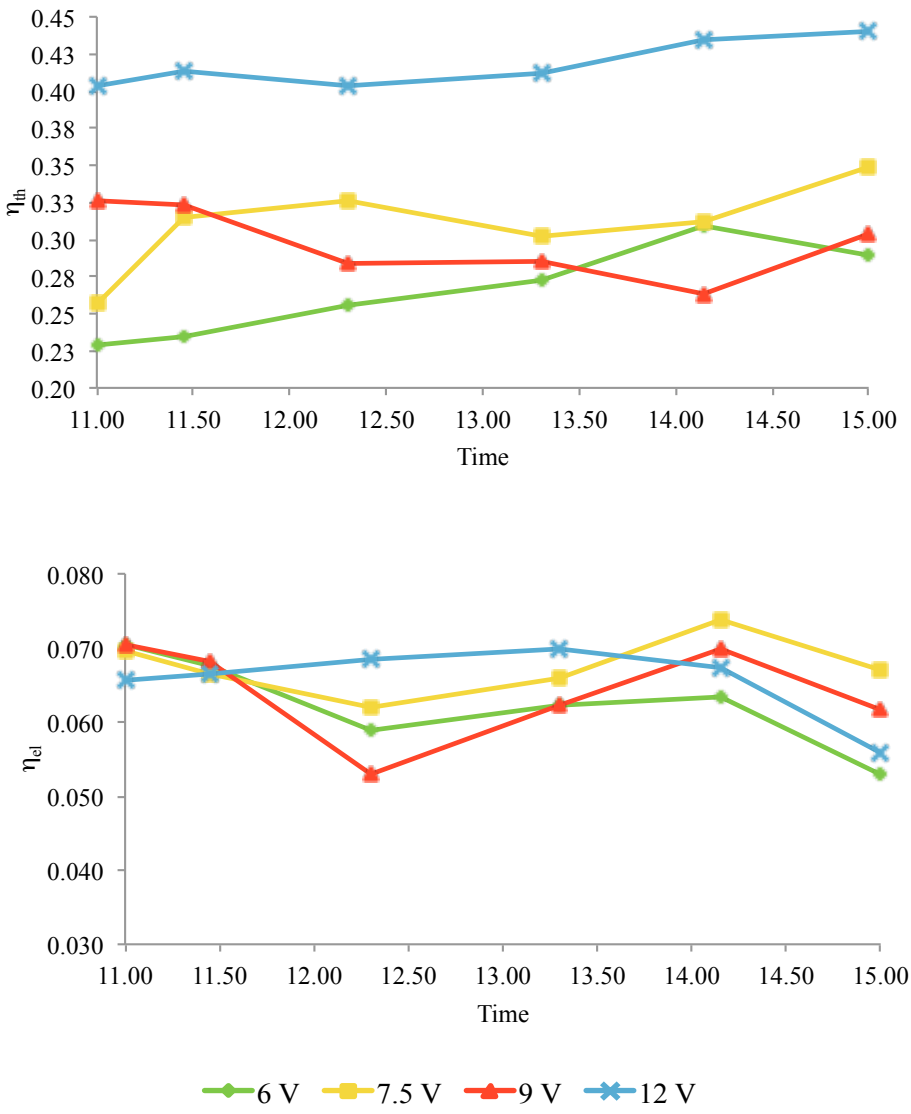

Fig 41: Thermal (top) and electrical (bottom) efficiency.

4.4 Comparison For The Vertical South-Facing Case

Sections 4.1-4.3 reported the several types of measurements that have been performed, which included the study of the prototype's behavior under different tilting conditions, at both fixed and tracking orientations, and under different airflow velocities. Since for the majority of residential and commercial buildings the façade are constructed vertically, the testing of the prototype in vertical position and at a fixed orientation represents the most suited configuration for common applications. In this section, a side-by-side comparison between the different seasons is provided for the vertical south-facing scenario. The results are given for the days of July 10th, November 25th and February 24th.

4.4.1 Thermal Results

In Fig 42 the hourly change of global solar irradiance on the window surface, average air temperature output, air temperature rise between the output and input vents and heat transfer rate are shown. As it can be seen in the figure, the solar irradiance for July 10th ranges from 90 W/m2 at 10:00 to 247.67 W/m2 at noon, and then drops in the afternoon to values ranging from 120-200 W/m2. The low solar input observed in the summer season is due to the high solar elevation, which was 75º at noon for July 10th, which causes a smaller horizontal component reaching the collector vertical surface. On November 25th, the solar altitude was instead 32.5º at noon, and much higher values were recorded: 650 W/m2 is the radiation at 10:00 and 860 W/m2 was the peak irradiance at noon, with an afternoon decrease from of 680 W/m2 at 14:00 to

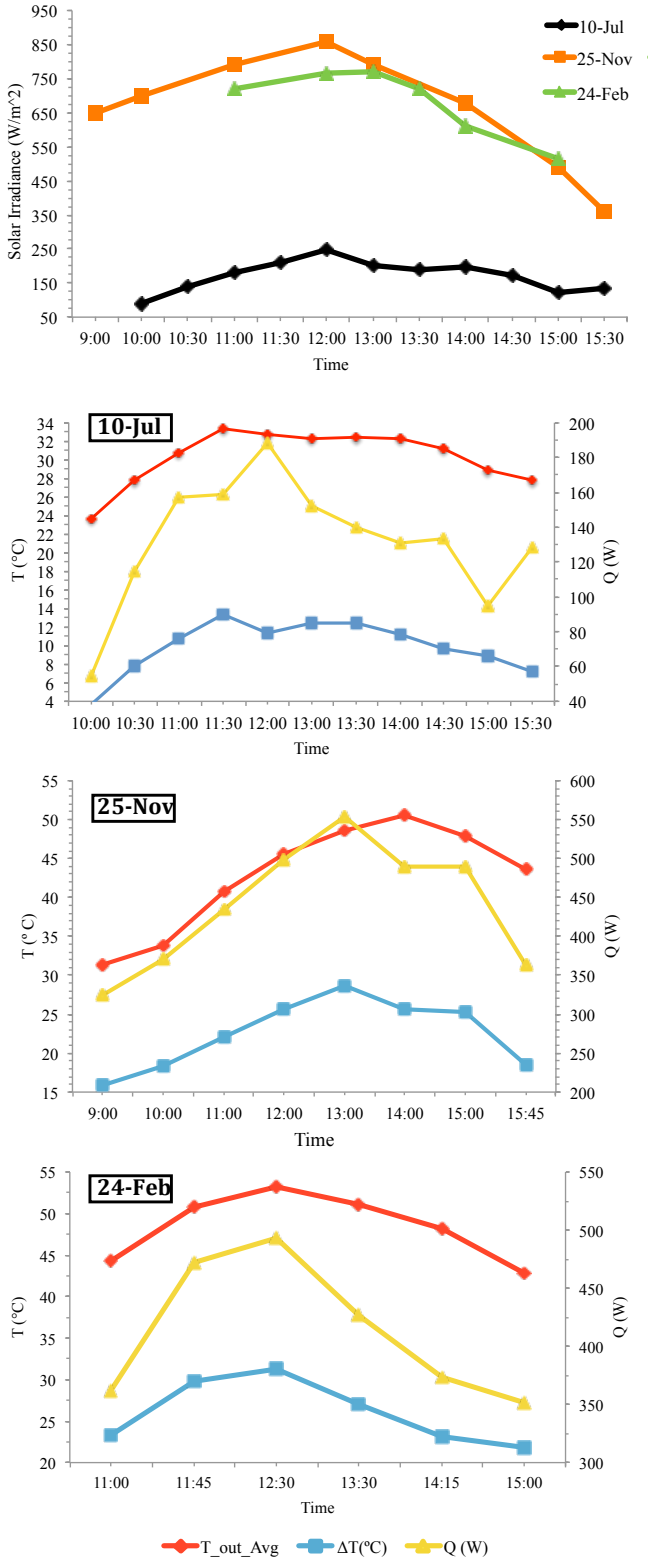

Fig 42: Hourly data of the solar radiation, temperature output, temperature rise and generated heat for the days of July 10th, November 25th and February 24th.

490 W/m2 at 15:00. Very similar values were measured on February 24th, with a peak of 765 W/m2 at noon, corresponding to a solar elevation of around 44º, and values in the 500-700 W/m2 range from 13:30 to 15:00.

It can be seen that the different solar inputs are reflected on the temperature and heat transfer rate profiles in the results. The output temperature reaches a maximum of 33.3ºC at 11:30 on July 10th, with values ranging from 30 to 32ºC for most of the day, while the maxima are 50.5ºC for November 25th and 53.2ºC for February 24th, with average values from 11:00 to 15:00 of 46.7ºC and 48.4ºC, respectively. The average air temperature rise between 11:00 and 15:00 are 11.2ºC for the summer, 25.4ºC for the fall and 26ºC for the winter results, with peaks of 13.3ºC, 28.6ºC and 31.2ºC, respectively. The heat generated on July 10th is most of the time within a narrow range of 100-160 W, with a peak of 188W at noon, while the increased temperature rise in the fall and winter seasons makes these results more than double for November 25th and February 24th, with average values from 11:00 to 15:00 of 476.7W and 412.9W, respectively, and peaks of 553W and 492.6W, respectively.

4.4.2 Electrical Results

Fig 43 shows the profiles of the electrical power generated and the average temperature on the back of the modules for November 25th and February 24th. The results are given for a PV array tilting of 90° with respect to the ground, that is the normal to the window and the normal to the PV array are parallel. In fall the lower solar altitude and lower modules temperature provide a higher photovoltaic generation, with an average of 24.5W from 9:30 to 14:30 and a peak of 29.5W. PV temperatures ranges

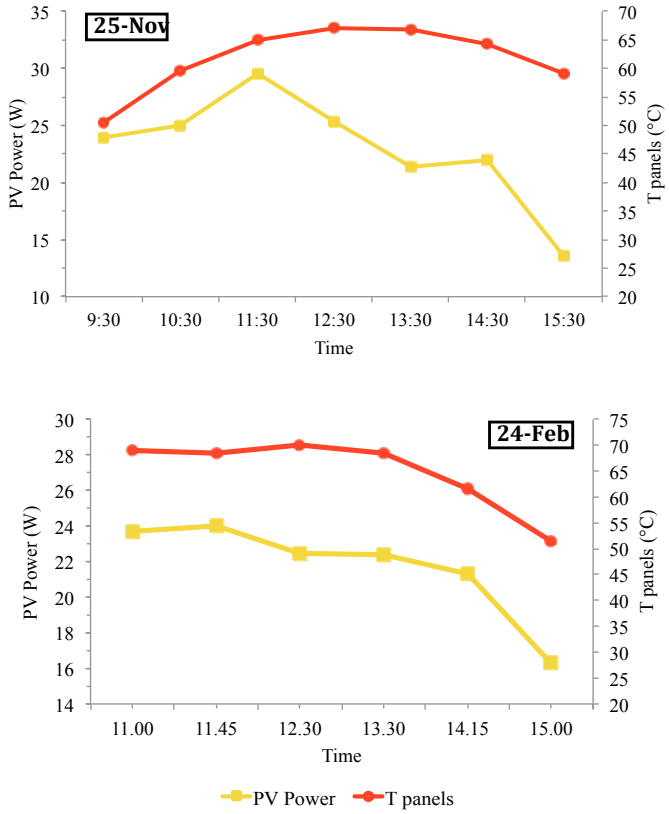

Fig 43: Hourly variation of average modules temperature and PV power output for November 25 (left) and February 24 (right).

from 50°C to 67°C, with an average of 64.5°C from 10:30 to 14:30. The electrical generation for 24.02.2015 is instead 22.8W on average from 11:00 to 14:15, with a peak of 24W at 11:45, and the average temperature in the same time range is 67.5°C, with a peak temperature of 70°C.

4.4.3 Efficiency

Fig 44 shows the thermal and electrical efficiency of the prototype for the different tested seasons. On July 10 the thermal efficiency remains very close to the 37-40% range, also due to lower operating temperatures that causes lower heat losses, while

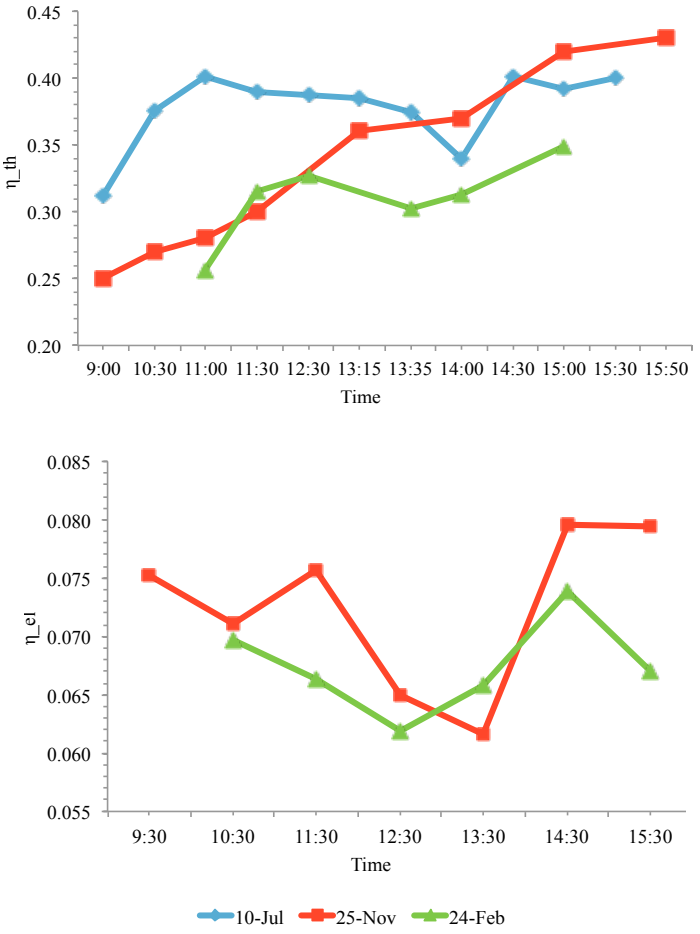

Fig 44: Thermal efficiency (left) and electrical efficiency (right) for the tested seasons.

greater differences occur in fall and winter, where values between 25% and 43% for November 25th and between 26% and 35% for February 24th are achieved.

The minimum and maximum values for the electrical efficiency are 6.16% and 7.96% for November 25th and 6.2% and 7.4% for February 24th, respectively, while the averages are 7.2% in fall and 6.7% in winter.

In order to improve the efficiency and achieve higher temperatures, the features of the current prototype need to be optimized. This includes designing a better absorber, which means enhancing the radiation captured by the PV array and improving the

heat transfer coefficient between the array and the air, in order to obtain higher heat collected by the airflow and lower PV temperatures, which is expected to increase both the thermal and electrical efficiency. The efficiency of the PV modules used has to be chosen according to the specific thermal and electrical requirements, since more efficient modules would convert a higher portion of radiation into electricity, but would also generate less heat and vice versa. The frame of the current design is made of aluminum, which is one of the main causes of heat losses, and therefore it requires further improvements with a better design and the use of different materials. Another component requiring optimization is the glazing system, which affects the solar radiation transmitted to the inside as well as the convective and radiative heat losses from the interior to the outside environment. The installation of additional glass panels and the use of low-emissivity or spectrally selective coatings may contribute to the system performances.

Chapter 5

Conclusions

In this work, the thermal and electrical performances of a prototype of an airflow window have been investigated. The prototype is a newly developed variant of a BIPV/T air collector, consisting of double glazed air cavities with PV blinds mounted within the glass panels, and it is designed as a modular unit to be applied to residential and commercial windows, window walls or to the whole façade of the building. Air from either inside or outside is circulated through the unit, which converts solar radiation in both electricity and heat, the latter being transferred to the air and put into use. With this new concept of "solar window", the glazed elements of the building's envelope not only perform their architectural and structural functions, but they also act as energy collectors, actively participating in the energy generation system of the building.

Electrical and thermal measurements were carried out under different testing conditions during summer, fall and winter months.

The lowest generation was obtained during the summer, due to the higher solar elevation angles that cause a smaller horizontal component of the radiation reaching the window surface. A vertical south-facing positioning of the unit resulted in an average temperature rise of only 10°C from bottom to top. Large improvements can be achieved by tracking the sun and tilting the window. However, tracking is not a practical solution for incorporating such collector into a building façade as it would be quite difficult to implement a tracking or tilting mechanism.

Conversely, the results for the winter testing showed much higher performances, due to smaller solar elevation angles, where the measured output temperature reached a maximum of 52.2°C under the optimal air speed of 0.58 m/s, with an average of 48.4°C, corresponding to a temperature rise of around 26°C on average and 31°C maximum.

The thermal efficiency ranges between 30 and 40%, while the electrical one remains quite constant at around 6-7%, with a generation of 20-25 W for the top PV array. The drop in electrical performance, with respect to a 12.5% rated efficiency of a single module and a 60 W rated electrical power of the array, is mainly due to the high operating module temperatures, which reach 70°C. Higher electrical performances could be achieved through the use of more efficient PV modules, though the effect that an increased electrical generation would have on the thermal output should be further investigated. Another way to improve the modules efficiency would be to place them on the bottom part of the window, where the temperature levels are lower, and hence they would operate more efficiently.

Bibliography

[1] M. Dabaieh and A. Elbably, "Ventilated Trombe wall as a passive solar heating and cooling retrofitting approach; a low-tech design for off-grid settlements in semi-arid climates", Solar Energy, vol. 122, pp. 820-833, 2015.

[2] "Monthly Energy Review - U.S. Energy Information Administration", Eia.gov, 2017. [Online]. Available: https://www.eia.gov/totalenergy/data/monthly/. [Accessed: 06 - Jun - 2017].

[3] "EIA - Annual Energy Outlook 2017", Eia.gov, 2017. [Online]. Available: https://www.eia.gov/outlooks/aeo/. [Accessed: 06- Jun- 2017].

[4] "Thermal Insulation", Solar Power Services Directory. [Online]. Available: https://www.solardirectory.com.au/power-saving/thermal-insulation. [Accessed: 14 - Dec- 2016].

[5] O. Saadatian, C. Lim, K. Sopian and E. Salleh, "A state of the art review of solar walls: Concepts and applications", Journal of Building Physics, vol. 37, no. 1, pp. 55-79, 2013.

[6] "Ecoedility » Blog Archive » Guadagno solare indiretto: sistemi a muro solare.", Ecoedility.it. [Online]. Available: http://www.ecoedility.it/e3news/?p=155. [Accessed: 22 - Feb- 2016]

[7] G. Gan, "Simulation of buoyancy-induced flow in open cavities for natural ventilation", Energy and Buildings, vol. 38, no. 5, pp. 410-420, 2006.

[8] B. Agrawal and G. Tiwari, Building integrated photovoltaic thermal systems for sustainable developments, 1st ed. Cambridge: RSC Publishing, 2011, p. 151.

[9] Y. Tian, and C.Y. Zhao, "A review of solar collectors and thermal energy storage in solar thermal applications." Applied Energy, vol. 104, pp. 538-553, 2013.

[10] J. Duffie and W. Beckman, Solar engineering of thermal processes, 4th ed. Hoboken, N.Y.: Wiley, 2013, pp. 3-41, 238.

[11] D. Goswami, Principles of Solar Engineering, 3rd ed. Hoboken: CRC Press, 2015, p. 130.

[12]"Solar hot water collectors", GreenSpec, 2017. [Online]. Available: http://www.greenspec.co.uk/building-design/solar-collectors/. [Accessed: 16 - Mar - 2017].

[13]A. Rabl, Active solar collectors and their applications, 1st ed. New York: Oxford Univ. Press, 1985, pp. 8-23.

[14]Deutsche Gesellshaft für Sonnenenergie, Planning and installing solar thermal systems, 2nd ed. London: Routledge, 2010, pp. 223-230.

[15]G. Tiwari, A. Tiwari and Shyam., Handbook of solar energy, 1st ed. Singapore: Springer Science+Busines Media, 2016, pp. 369-373.

[16]H. Henning, M. Motta and D. Mugnier, Solar cooling handbook, 1st ed. Vienna: Ambra V, 2013, pp. 61-63.

[17]S. Kalogirou, Solar energy engineering: processes and systems, 2nd ed. Academic Press, 2013, pp. 125-133.

[18]M. Wolf, "Performance analyses of combined heating and photovoltaic power systems for residences", Energy Conversion, vol. 16, no. 1-2, pp. 79-90, 1976.

[19]M. Alonso García and J. Balenzategui, "Estimation of photovoltaic module yearly temperature and performance based on Nominal Operation Cell Temperature calculations", Renewable Energy, vol. 29, no. 12, pp. 1997-2010, 2004.

[20]S. Kalogirou and Y. Tripanagnostopoulos, "Hybrid PV/T solar systems for domestic hot water and electricity production", Energy Conversion and Management, vol. 47, no. 18-19, pp. 3368-3382, 2006.

[21]J. Tonui and Y. Tripanagnostopoulos, "Improved PV/T solar collectors with heat extraction by forced or natural air circulation", Renewable Energy, vol. 32, no. 4, pp. 623-637, 2007.

[22]M. Hasan and K. Sumathy, "Photovoltaic thermal module concepts and their performance analysis: A review", Renewable and Sustainable Energy Reviews, vol. 14, no. 7, pp. 1845-1859, 2010.

[23]D. Harvey, A Handbook on Low-Energy Buildings and District-Energy Systems, 1st ed. Hoboken: Taylor and Francis, 2012, pp. 479-482.

[24]P. Charalambous, G. Maidment, S. Kalogirou and K. Yiakoumetti, "Photovoltaic thermal (PV/T) collectors: A review", Applied Thermal Engineering, vol. 27, no. 2-3, pp. 275-286, 2007.

[25]N. Singh Kapany, "Solar Window apparatus and method", U.S. Patent 8,046,960 B1, issued November 1, 2011.

[26]P. Kamkird, N. Ketjoy, W. Rakwichian and S. Sukchai, "Investigation on Temperature Coefficients of Three Types Photovoltaic Module Technologies under Thailand Operating Condition", Procedia Engineering, vol. 32, pp. 376-383, 2012.

[27]J. Dunlop, Photovoltaic systems, 3rd ed. Orland Park, IL: American Technical Publishers, Inc., 2012, pp. 131-142, 260-269, 308-318.

[28]S. Kolsi, H. Samet and M. Amar, "Design Analysis of DC-DC Converters Connected to a Photovoltaic Generator and Controlled by MPPT for Optimal Energy Transfer throughout a Clear Day", Journal of Power and Energy Engineering, vol. 02, no. 01, pp. 27-34, 2014.

[29]O. Mørck and S. Hastings, Solar air systems, 1st ed. London: James & James Ltd, 2000, p. 133.

[30]Y. Çengel, Heat transfer. Boston, Mass.: WBC McGraw-Hill, 1998, pp. 6-20.

[31]"PVEducation", Pveducation.org, 2013. [Online]. Available: http://www.pveducation.org. [Accessed: 21 - Nov- 2016]

[32]E. Skoplaki and J. Palyvos, "On the temperature dependence of photovoltaic module electrical performance: A review of efficiency/power correlations", Solar Energy, vol. 83, no. 5, pp. 614-624, 2009.

[33]A. Luque and S. Hegedus, Handbook of photovoltaic science and engineering, 1st ed. Chichester, West Sussex, U.K.: Wiley, 2012, p. 113.

Other general references

F. Incropera and D. DeWitt, Fundamentals of heat and mass transfer, 5th ed. New York: Wiley, 2002.

S. Sukhatme and J. Nayak, Solar energy principles of thermal collection and storage, 3rd ed. New Delhi: Tata McGraw-Hill, 2008.

S. Kornher and A. Zaugg, The complete handbook of solar air heating systems, 1st ed. Emmaus, Pa.: Rodale Pr., 2006.

R. Hastings, Passive solar commercial and institutional buildings, 1st ed. Chichester, U.K.: Wiley, 1994.

U. Eicker, Energy efficient buildings with solar and geothermal resources, 1st ed. West Sussex, U.K.: Wiley, 2014.

J. Kreider and F. Kreith, Solar heating and cooling, 1st ed. Washington: Hemisphere Pub. Corp., 1982.

G. Tiwari and S. Dubey, Fundamentals of photovoltaic modules and their applications. Cambridge: Royal Society of Chemistry, 2010.

H. Haberlin, Photovoltaics system design and practice, 1st ed. Hoboken, N.J.: Wiley, 2012.